Mechanical Modification of Cells by Pressure Waves and Its Application to Traumatic Brain Injury

by

Kadeem Dennis

Thesis submitted to the
Faculty of Graduate and Postdoctoral Studies
In partial fulfillment of the requirements
For the M.A.Sc degree in
Mechanical Engineering

Department of Mechanical Engineering
Faculty of Engineering
University of Ottawa

Abstract

Recently there has been interest in determining what happens to the human brain during a traumatic brain injury (TBI). The blast wave created by explosive devices, such as landmines, is one of the most common causes of TBI. The purpose of this study is to investigate the link between an explosion and a cells reaction to a blast wave on a time scale of a few hours. Three different types of cells were tested by pressure waves exposure, fibroblasts (3T3), epithelial cervical cancer (HeLa), and canine epithelial kidney cells (MDCK). Fluorescent images of the cells before and after pressure wave exposure were used to determine how much damage cells have suffered. 3T3 cells showed the most cellular modification while HeLa and MDCK were more resilient. A simple scaling model is proposed to relate the cellular modification to the shock strength.

Acknowledgements

I would like to thank Dr. Matei Radulescu for providing this opportunity and supervising my work. I want to thank Defence Research and Development Canada for funding this research. Thanks to Dan Modulevsky, Dr. Pelling, and everyone at the Pelling Lab for providing cells and helping me learn about biophysics. I want to thank everyone in DRDL for their help in experiments. Thanks to the Mechanical Engineering machine shop staff for teaching me about real-world manufacturing and machining. Finally I would like to thank my family and friends for their support during this degree.

Dedication

This is dedicated to the future.

Table of Contents

List of Tables

List of Figures

Chapter 1

Introduction

1.1 Overview

The goal of this thesis is to investigate the link between an explosion and its effect on cells on a time scale of a few hours after exposure. Specifically of interest are explosions that produce traumatic brain injury (TBI). In military conflicts, explosive devices such as landmines are capable of producing a TBI. When detonated, an explosive device produces a shock wave, shrapnel, and blast wind. Shrapnel traveling at high-speed can lead to puncture and laceration injury. Blast wind is the hot gas produced by reacting explosive material being advected behind the lead shock wave. Scorched objects and burn injuries are common results of blast wind exposure. The shock wave however may not have an immediately visible effect. A traumatic brain injury produced by a shock wave may go unnoticed until complications occur or chronic symptoms develop.

Blast-induced TBI (bTBI) is a complex phenomena that encompasses several branches of science. This includes the biology and chemistry of the human brain in addition to physics involved in high-speed blast loading. Presently there is no complete understanding of the mechanism leading to injury in blast-induced TBI. Indeed given the complexity of bTBI, no well established model currently exists. In constructing a model, one classical approach is to build upwards from the most simple phenomena. In studying bTBI, this means analyzing a single cell and shock wave interaction. The first step is to determine which phenomena at a cellular level contribute to TBI produced by a shock wave. We seek to determine what happens to a cell when a shock wave interacts with it.

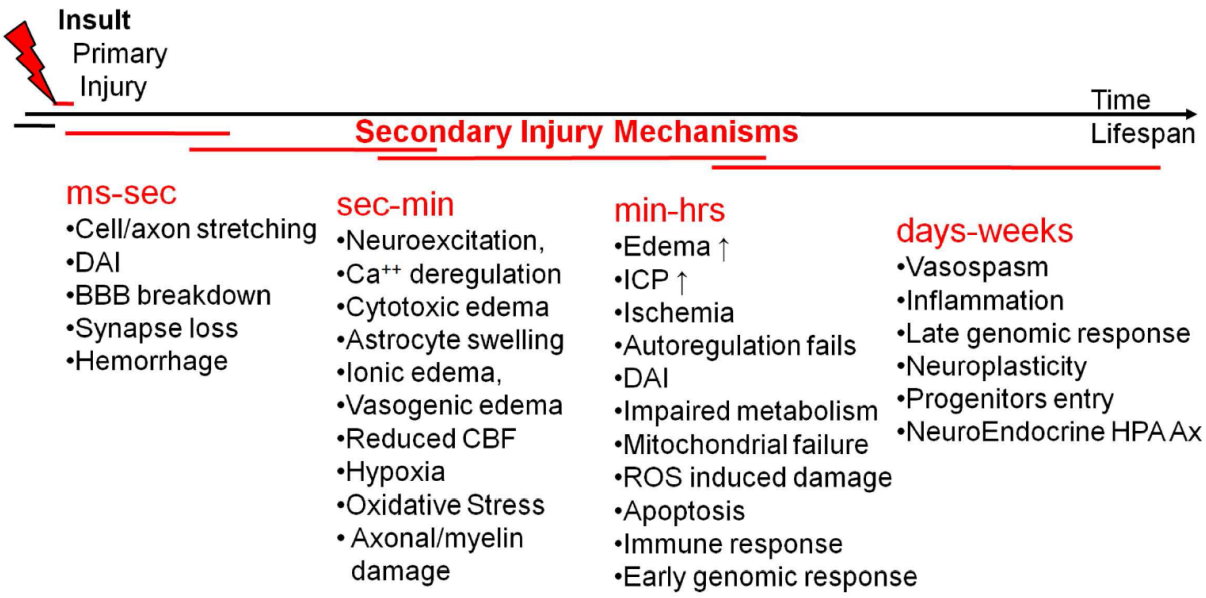

Figure 1.1: List of secondary injuries associated with TBI adapted from Gupta [1].

1.2 Background

1.2.1 Traumatic Brain Injury

Traumatic brain injury (TBI) is defined as a non-degenerative, non-congenital insult to the brain from an external mechanical force [5]. It can lead to permanent or temporary impairment of mental and physical functions. The causes of TBI can be separated into two classes. The first is penetrative injury as a result of foreign objects making a hole in the skull and damaging brain tissue. The second is non-penetrative injury created from the head undergoing exposure to a blast, strong impact, or sudden acceleration. TBI produced via non-penetrative means may occur during a car crash where a drivers' head strikes the steering wheel. In the case of a sudden acceleration, such as shaken baby syndrome, TBI is produced from the acceleration an infant's brain suffers when shaken [6]. In military conflicts, explosives create a blast wave that leads to TBI.

When a traumatic brain injury occurs, the brain and human body respond on multiple time-scales. The very quick responding systems begin a biophysical sequence of events leading to a number of secondary phenomena. Figure 1.1 adapted from Gupta lists some of the injuries associated with TBI and when they occur [1].

Within milliseconds to seconds after injury, several mechanical and hydrodynamic phenomena occur. Two of the first things to happen are neuron deformation and damage to brain interfaces such as the blood brain barrier. Diffuse axonal injury (DAI) is a common injury resulting from TBI. It happens within seconds of the primary injury due to rapid mechanical loading of brain tissue and often makes a person lose consciousness. Hydrodynamic fluid

Figure 1.2: A VS-50 landmine next to a wrist watch. Despite being very small it can generate a shock wave strong enough to produce a TBI. Picture taken by Clark [2].

exchange between brain structures leads to ionic edema and reduced nutrient supply to affected regions within minutes of injury. It is not until several minutes to hours after injury that apoptosis, cellular death, begins. At around the same time, the human immune system begins responding to the injury. Inflammation perceived as a headache may not appear until days after the injury [1].

Over 1 million Americans annually suffer a mild TBI without fainting and have no need to be hospitalized [7]. Most people recover from injury with no chronic symptoms however; persistent headaches, fatigue, and memory recall deficits are all common. In very rare cases, a mild TBI can be fatal several hours after primary injury [8]. Presently there is controversy surrounding diagnosis and treatment of TBI. Significant research into understanding how TBI happens in impact has yielded a very limited understanding of the injury mechanism [1, 9].

There is even less research and understanding of blast related TBI. The on-going conflicts in the Middle East have helped generate interest in blast-induced TBI. Two-thirds of war-zone evacuations are due to blasts, and it is suspected 20% of personnel have some form of TBI [10, 11]. The prevalence of blast-injury is partly due to the widespread use of improvised explosive devices (IEDs) and landmines such as the one seen in Figure 1.2. These devices are easily concealed and capable of delivering a blast-wave to surrounding people [12].

There are a number of pathways a blast wave can create mechanical loading in the brain. The wave can enter the brain directly through foramina, which are holes in the skull. Motion of the brain as a result of the blast wave generates localized compression and shear. Deformation of the skull results in transmitted stress to the brain. Lastly, compression of other body parts produces a stress wave that enters the brain via blood vessels.

As a blast wave impacts the head, the skull deforms, which transmits compression waves through cerebrospinal fluid to the brain. These waves travel at the sonic velocity of the skull at ∼1500 m/s [1]. The human brain is characterized by a 10^1 centimeter length scale. This defines the time-scale of wave propagation and compressive loading on the order 10^{-1} microseconds. For cells that are a few micrometers in size the time scale of shock passage is on the order of nanoseconds. Transverse shear waves are also generated by compression waves which travel much slower [1]. The shear load from these waves may contribute to damage in the form of crack propagation in the skull [13]. These same phenomena occur if the incident wave enters the skull via foramina.

Subsequent to the high-speed loading from blast waves is the damage produced by the resulting brain motion. Both translational and angular acceleration of the brain is created by blast waves. These lead to diffuse axonal injury, bruising, and bleeding inside the brain (hematoma) [14]. Linear motion of the brain displaces cerebrospinal fluid as the brain advances toward the skull. It is possible for the brain to impact the skull and cause brain injury. Similarly, angular motion can also lead to brain-skull impact which has been shown to be more severe than linear impact [14, 15].

The brain is fed by several large blood vessels connecting to the fluid-filled spinal column. Sudden deformation of different parts in the body generates stress waves that can enter the brain through blood vessels [1, 16]. The propagation speed of these waves is ∼10 m/s. For a region 10^1 meters from the brain, such as the human thorax, damage resulting from these stress waves entering the brain will occur on a time scale of 10^1 seconds.

1.2.2 TBI Research

Blast-induced traumatic brain injury (bTBI) is a complex multi-disciplinary phenomena. It happens on multiple time-scales; from the nanosecond time scale of a shock wave passing through a cell to the biological response after several hours. A complete understanding of bTBI depends on work in biophysics, medicine, chemistry, and physics. There has been research both experimentally and numerically analyzing TBI.

Experimentally studying TBI has produced a number of works utilizing animals and human head analogues [17, 18, 19, 20, 21]. In order to reproduce blast waves, gas shock tubes are a popular choice as the blast wave profile can be easily controlled [17, 22]. While a human head analogue is useful for gathering data such as pressure distribution, it cannot replicate biological response. The only way to study the brain in its natural environment, *in vivo*, is through the use of animal experimentation.

Whole-body blast injury (WBBI) is a common technique where an entire living animal is exposed to a blast. Cernak et. al. performed WBBI experiments on lab rats with shock waves having a mean peak overpressure of 338 kPa in air [17]. The blast wave was produced by a 1 m inner diameter by 39 m long shock tube. WBBI experiments were performed by placing an immobilized lab rat inside the shock tube. At 3 hours, 24 hours and, 5 days after exposure, rats were subjected to a cognitive test to measure brain function before being dissected to determine injury severity. Neurons in the hippocampus 24 hours after blast

showed an increased quantity of vacuoles, water-filled organelles within cells, and increased spacing between nerves. Before blast exposure, rats were able to complete 85% of cognitive tests. At all times after testing, lab rats were only able to complete 50% of tests indicating brain damage from the blast persisted until 5 days after exposure.

Kato et. al. studied brain injury by using a silver azide reaction to drive a shock wave directly into a rat's brain instead of using the WBBI technique [18]. There were two shock conditions tested. The low pressure condition had an average overpressure of 1 MPa while the high pressure condition had an average of 12.5 MPa where both pressures were measured in saline solution. At 4 hours, 24 hours and, 72 hours after exposure the test rats were dissected. In response to the low pressure shock wave, no significant brain hemorrhaging was found in any of the rats. In addition, neuron nuclei were elongated and shaped into a spindle 24 hours after exposure. In contrast, the high pressure shock wave produced hemorrhaging at 4 hours, and worsening contusional brain injury at 24 and 72 hours after exposure.

Kato's results suggest the brain has a threshold of injury lower than 1 MPa. While Cernak never measured pressure inside the skull, cerebrospinal fluid is nearly incompressible. From shock wave and material interface theory, it is expected the peak intercranial pressure was higher than the 338 kPa measured in air. *In vivo* experiments with animals are able to define damage thresholds and study behavioral effects of blast waves however, there is no existing method of scaling these results to humans.

Analyzing TBI from a computational approach requires applying models from several fields of science. The human head, brain, and all of its pathways must be constructed. A complete cardiovascular system model is needed in order to capture the effects of stress waves entering the brain via blood vessels. Capturing blast wave dynamics requires the use of computational fluid dynamics (CFD) models. A number of models exist that address these fields individually, however there is no comprehensive model [3, 22, 23, 24, 25, 26].

Recently there has been work in bringing together blast-wave CFD and human head models to study TBI. Wang et. al. performed a study that brought together FEM of the human brain from MRI data with CFD simulation of the blast-wave [3]. A 220 kPa peak overpressure in air shock wave was sent towards the head model in a closed volume. The human model contained a number of pressure measurement points to monitor pressure evolution within the skull.

During the blast it can be seen in Figure 1.3 that once the shock wave interacts with the brain at $\sim$0.5 ms the brain surface pressure rises up to around 500 kPa. After which the pressure fluctuates rapidly with peaks ranging between 500 kPa and 1 MPa. In order to calculate the brain damage produced, collected pressure data was used to simulate loading on brain blood vessels. It was predicted that the shock loading and subsequent brain motion was sufficient to damage blood vessels of all sizes in the brain.

The results of numerical studies must be validated against experimental work in order to further improve modeling. The blood vessel damage predicted is known to be the mechanism for hemorrhaging seen in experiments [27]. While it is currently possible to capture the fast-evolving physics, the slow biological response, governed by neuron behavior, is not presently within reach. At the microscopic scales there are several models of neuron behavior however,

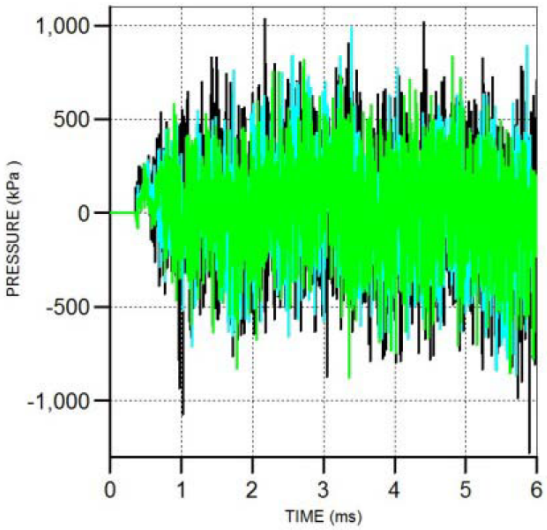

Figure 1.3: Pressure vs time history of three points on the brain surface. From Wang et. al. [3].

as there is no complete understanding of cellular mechanics, a full biomechanical cell model does not exist [1, 28].

Laboratory grown, *in vitro*, cells remove much of the variability inherent to animal cells *in vivo*. Data collection from these cells is also much easier as there is direct access for optical and physical measurement. *In vitro* neurons have been used to study brain injury. Instead of using a blast wave however, the wave is replaced by one of several stand-ins such as stretching or shearing in experimental work, and in numerical studies a sinusoidal wave has been used [22, 29, 30].

Tamagawa et. al. utilized a two-cell model to study cell deformation in response to a shock wave [22]. The cells were treated as elastic spheres filled with liquid. The shock wave was broken down into a sine wave with amplitude set at 100 Pa and frequency less than 100 MHz. Red blood cells were modeled using their cell membrane thickness and cell radius. Poisson's ratio and the bulk modulus of the internal liquid were held constant at 0.499 and 1 GPa respectively. The effect of the cell membrane's elastic modulus and cell spacing on cell deformation was evaluated. The deformation of the tested cells was found by calculating the frequency response. It was found that increasing the elastic modulus of the cell membrane from 3 MPa to 300 MPa decreased cell deformation and increased the cell's natural frequency. Increasing cell size at constant membrane thickness was shown to increase deformation. As cells were moved together, decreasing cell spacing, one cell would interact with the other causing both to move. This simulates interactions occurring in tissues where cells are densely packed. The results of Tamagawa's study mathematically demonstrate the effect of cell type, which defines size, elastic modulus, and spacing on cellular response to shock waves.

Mechanical shearing of neurons has been used by LaPlaca et. al. to study brain injury [29]. Cells harvested from lab rats were grown into a three-dimensional culture before being loaded into a parallel-plate shearing system. Two strains were tested, 0.25 and 0.50, at multiple

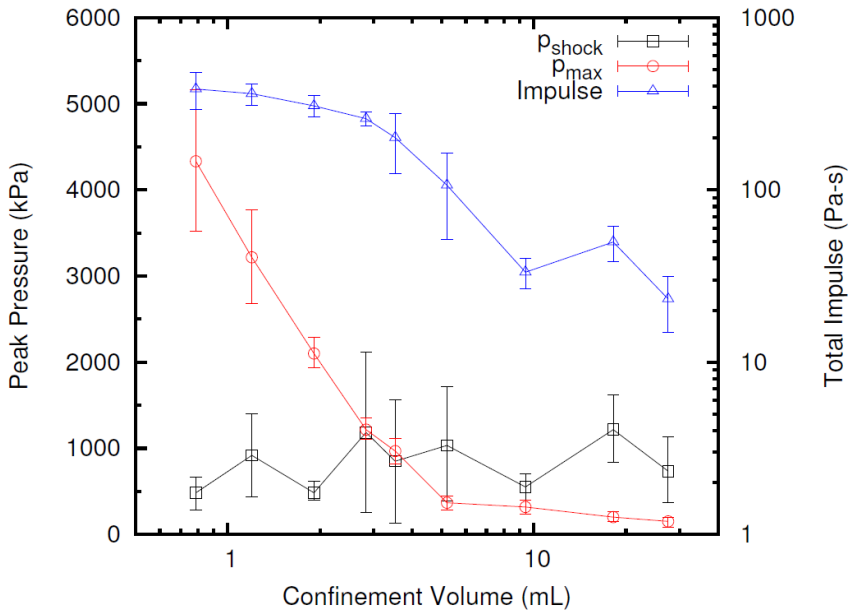

Figure 1.4: Pressure and impulse vs confinement volume plot produced by aluminum bismuth-oxide thermite reaction. Adapted from Apperson et. al. [4].

strain rates. Two different kinds of brain cells, astrocytes and neurons, were used. Astrocytes have several roles in the brain such as transmitting signals and helping to keep neurons supplied with nutrients. Cell viability was measured 24 hours after loading. Neurons subjected to 0.50 strain at 20 s^{-1} and 30 s^{-1} strain rates showed 40% viability indicating significant cell death. It was found that astrocytes also showed 40% viability in response to 0.25 and 0.50 strain at 20 s^{-1} strain rate. At the low strain rate, 1 s^{-1}, no decrease in viability from control data was found. LaPlaca's results suggest that cell death depends more on strain rate than applied strain.

Recently Apperson et. al. utilized shock waves produced from reacting thermite powder in a closed volume to attempt transfection of various cells and tissues [4]. Nano-scale powders of aluminum and bismuth oxide were reacted generating a shock wave traveling through the transfection chamber. By varying the cell housing container volume, the maximum pressure and total impulse were controlled as shown in Figure 1.4.

The shock pressure was relatively constant at ~1 MPa. Both the maximum pressure and impulse decreased as confinement volume increased. Results showed chicken primary cells, cardiomyocytes, had 99% transfection and survival rates. Three kinds of cancer cells, HeLa, HL-60, and HT-29, in addition to spinal cord and artery tissues were also successfully transfected. No structural changes in the transfected cells were noted.

1.3 This Study

The transfected cells were shown by Apperson to survive a 1 MPa shock wave while it was shown that the same pressure pulse causes structural changes in neurons. The affected neurons led to a decrease in cognitive performance of lab rats. The mechanism that relates cellular modification to macroscopic change is not clear as there is no complete understanding of cellular biomechanics. It is of interest to characterize the response of *in vitro* cells to pressure waves in the context of injury. The goal of this work is to investigate the link between an explosion and the cellular response to a blast wave on a time scale of a few hours.

This study characterizes the response of *in vitro* cells to pressure waves. Aluminum mixed with copper(II)-oxide is prepared as the reactive thermite mixture. Experiments are performed in a one-litre underwater blast chamber designed and built by Maines that replicates the pressure signatures found by Apperson [31]. An exploding wire technique to produce underwater pressure waves is discussed and wave characteristics detailed. Three different kinds of *in vitro* cells are exposed to pressure waves from thermite reactions: epidermal fibroblasts (3T3), cervical cancer epithelial (HeLa), and dog kidney epithelial (MDCK). Cellular modification is monitored by observing the condition of actin filament at various time intervals after pressure wave insult. A method of anticipating cellular modification based on the shock strength is discussed and compared with experimental results.

This thesis is organized as follows. Chapter 2 presents the experimental setup and procedure. Results of pressure wave analysis and actin filament modification is in Chapter 3. A method of predicting cellular modification based on shock strength is presented in Chapter 4. Lastly, Chapter 5 summarizes the results and draws conclusions from this investigation.

1.4 Cellular Biology Background

In later chapters, results show that actin filament was modified in cells. This section introduces background knowledge on the function and purpose of actin microfilament in cellular biology to inform non-specialist readers.

Cells in their natural environment are subjected to a wide variety of mechanical stresses such as compression on bone cells and fluid shear on the endothelial cells that make up blood vessel walls. These cells, like all cells, respond to applied loads, communicate with neighboring cells, and move as needed. Actin filament plays an important part in both cellular mechanics and sensing. Actin filament is a polymer made of G-actin that contain the globular actin protein and adenosine diphosphate (ADP). Actin microfilament is a single helix created by repeated addition of G-actin monomers.

Microfilaments have polarity. At the +End, filament grows 5 to 10 times faster than at the -End [32]. In laboratory conditions, filament growth rate is controlled by the local concentration of G-actin [32]. Below a minimum concentration, the -End of a filament may

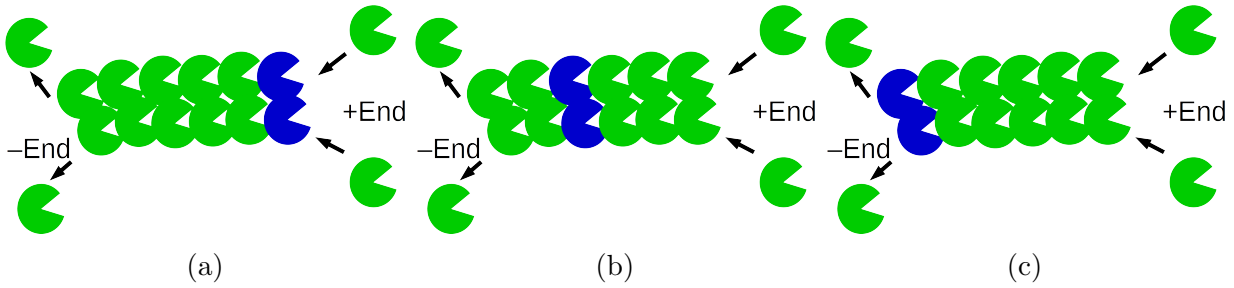

Figure 1.5: The actin filament treadmilling process.

disassemble and its G-actin monomers translate to the +End. This is a process known as treadmilling sketched in Figure 1.5.

Actin treadmilling begins in Figure 1.5a where a pair of monomers highlighted in blue bind to the +End of an existing filament. More G-actin is then added at the +End while at the -End G-actin monomers break off as shown in Figure 1.5b. This process advances G-actin towards the -End in Figure 1.5c. Treadmilling keeps the filament length constant while allowing it to advance towards the +End while individual G-actin monomers move closer to the -End [32].

In cells, the activity of proteins play a large role in microfilament behavior. Capping proteins can attach to the filament ends to inhibit further growth [32]. *Gelosin* and *severin* are proteins that act to cut existing filament and promote depolymerization [32]. *Thymosin* acts to prevent G-actin monomers from joining the helix and in contrast *profilin* promotes filament formation [32]. As the polymer grows it encounters other actin strands and cross-links to form a complex actin network connecting numerous points within a cell. Arp2/3 allows a filament to branch into daughter filaments that can push on the cell membrane to drive cell migration [32]. The interaction of actin filament and the myosin protein family enables processes such as muscular contraction and endocytosis [32].

The cell cytoskeleton is a dynamic structure containing microfilament, intermediate filament and microtubules. As a cell responds to loading, moves, or divides via mitosis the cytoskeleton reforms and transmits loads as needed. Focal adhesions enable cells to sense their surroundings. Loads entering through focal adhesions are transmitted to the actin filament and distributed through the cell [28]. Deformation of the cell leads to a rearrangement of the actin network through disassembly and reassembly. It has been shown that actin filament will dynamically arrange itself in the direction of a shear load [28].

When actin is allowed to polymerize in laboratory solution the fluid viscosity increases as the filaments become entwined [32]. Similarly, the actin network's structure produces a number of viscoelastic behaviors in cells such as load-dependent stiffening and relaxation [28]. When exposed to cyclic loading cells adapt to the environment and become increasingly insensitive to the applied stress [33]. It was shown this behavior was caused by actin filament network remodeling. Actin conditions also affect the elastic modulus of the cell as complete depolymerization causes a decrease in elastic modulus [28].

Chapter 2

Experimental Methods

In this chapter, details of the experimental setup and procedure are discussed. First, the underwater blast chamber and measurement techniques are described. Thermite powder preparation and isolation is presented next. This is followed by the exploding wire setup. Next, the steps to produce cell culture dishes are detailed. Lastly, the full procedure of one experiment is reviewed.

2.1 Setup

2.1.1 Underwater Blast Chamber

A 1.06-L-combustion vessel designed and built by Maines was used for experiments [31]. Made from aluminum (6061-T6) it can withstand 50 MPa internal pressure and has internal dimensions measuring 101.6 x 101.6 x 95.25 mm. Using two optical grade acrylic windows, visualization of the explosion chamber can be performed. Six multi-purpose plugs line the chamber sides. One is used for holding the ignitor plug while the other five allow for pressure measurement and fluid-handling as shown in Figure 2.1a. Two kinds of pressure transducers were used. A wall-mounted sensor (PCB 113B24) with a 1 μs rise time and an adjustable freefield sensor (Neptune Sonar T11) with a 4 μs rise time.

The ignition for experiments was performed with a spark plug mounted in a large threaded plug which fits into the chamber's top port as shown in Figure 2.1b. Thermite ignition was created by resistive heating of a tungsten wire embedded in thermite powder. A DC bench power supply (BK Precision 1550) capable of producing up to 36V and 3A provided energy for ignition.

A trigger unit (BNC 575 Pulse Generator) was used to synchronize ignition with data acquisition as shown in Figure 2.2. First, the National Instruments DAQ unit (PCI-6133) is given a signal from the trigger unit to begin recording data. Next, a signal is sent to an electronic switch initiating thermite ignition by the power supply. Pressure data acquired from the

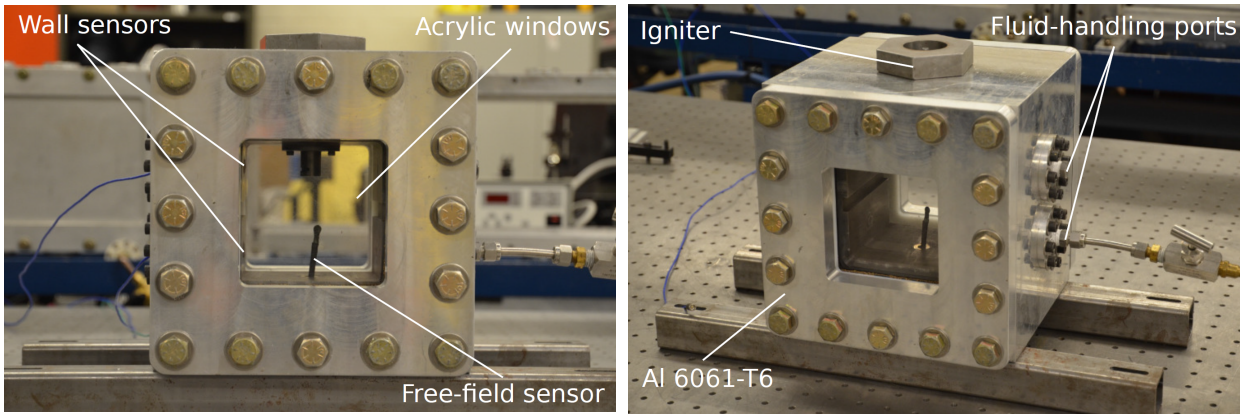

(a) (b)

Figure 2.1: Parts of the underwater explosion chamber built by Maines. Figure 2.1a shows the optical access as well as pressure sensor placement while Figure 2.1b shows the location of fluid-handling ports.

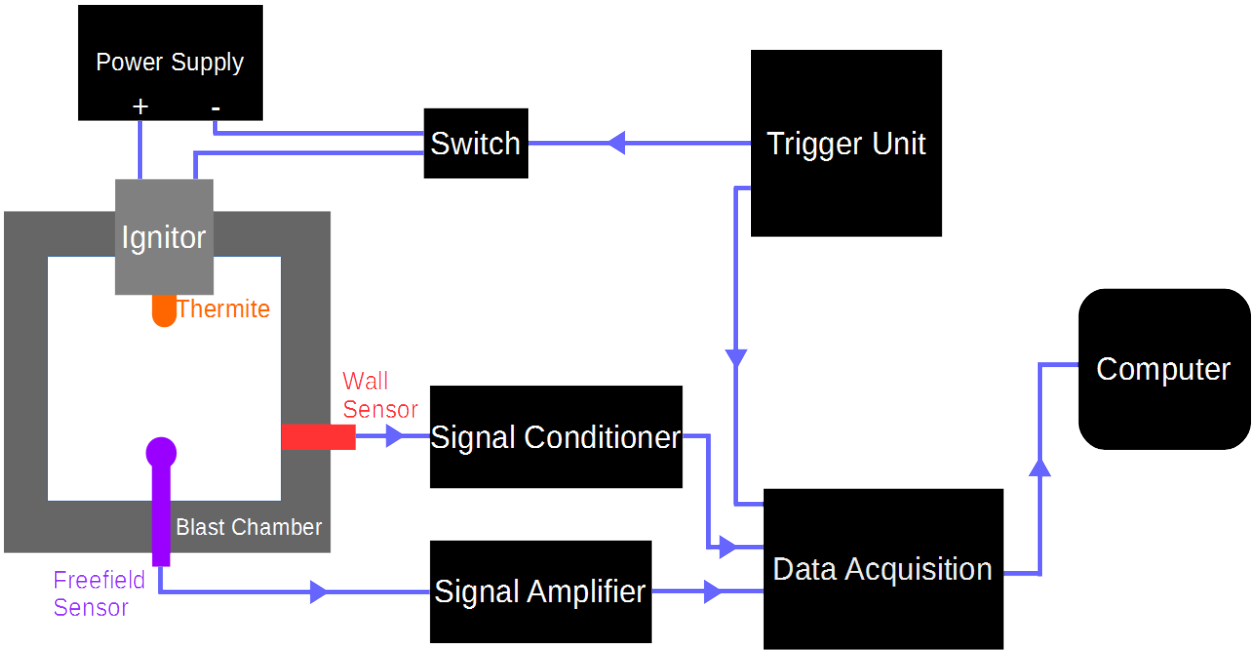

Figure 2.2: Sketch of the data acquisition process and equipment.

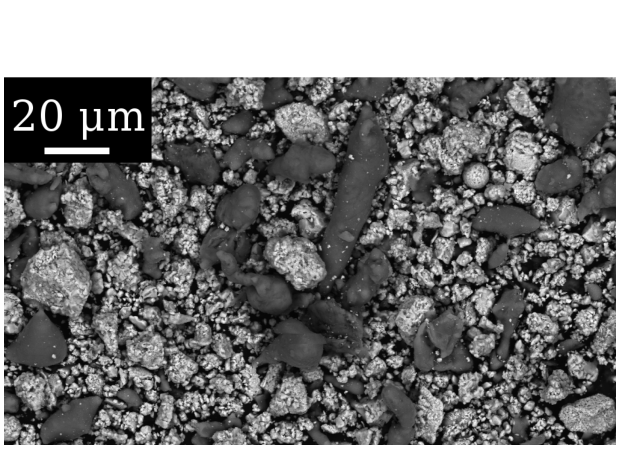

(a)

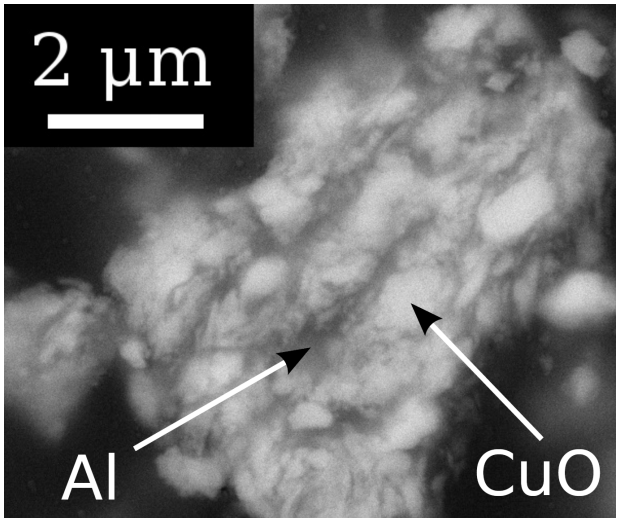

(b)

Figure 2.3: Scanning electron microscope images of unmilled and milled aluminum copper(II)-oxide thermite. Figure 2.3a shows unmilled thermite where the dark grey regions correspond to aluminum and the light gray is copper(II)-oxide. Figure 2.3b shows the particle structure after 16 minutes of milling. Pictures taken by Maines.

wall sensors passes through a signal conditioner (PCB Model 482C05) before reaching the DAQ connected to a computer. Data from the freefield sensor passes through an amplifier (Kistler Model 5004) before reaching the same DAQ unit. A LabView program was used to record acquired data and control signal sampling rate.

2.1.2 Thermite Preparation

Two thermite mixtures were used in this study. Both are blends of aluminum (Al, Atlantic Equipment Engineers AL-101, 99.9% pure, -325 mesh) and copper(II)-oxide (CuO, Atlantic Equipment Engineers CU-602, 99.9% pure, 1-5 μm) at stoichiometric proportions of 2:3 by mole aluminum to copper(II)-oxide. The powders were sifted to ensure particle sizes of less than 32 μm. One mixture is formed by using an arrested reactive milling (ARM) technique established by Maines for underwater explosions [31]. The milled powder had ARM performed for 16 minutes. The other mixture tested is unmilled hand-mixed thermite powder.

The scanning electron microscope images in Figures 2.3a and 2.3b show how ARM produces clearly defined sub-micron scale layers of aluminum and copper(II)-oxide. The ARM technique increases reaction speed without creating products indicative of a partial reaction in the milling process. It has been shown milled aluminum copper(II)-oxide thermite has a much higher flame speed and drives higher underwater shock and maximum pressures, summarized in Table 2.1 [31]. Milling this thermite mixture increases the maximum pressure from 880 kPa to 965 kPa while the shock pressure sees a much larger increase from 270 kPa

Table 2.1: Comparison of pressure wave characteristics for milled and unmilled thermite found by Maines.

Property	Unmilled	Milled
Shock Pressure (kPa)	270	450
Max Pressure (kPa)	880	965

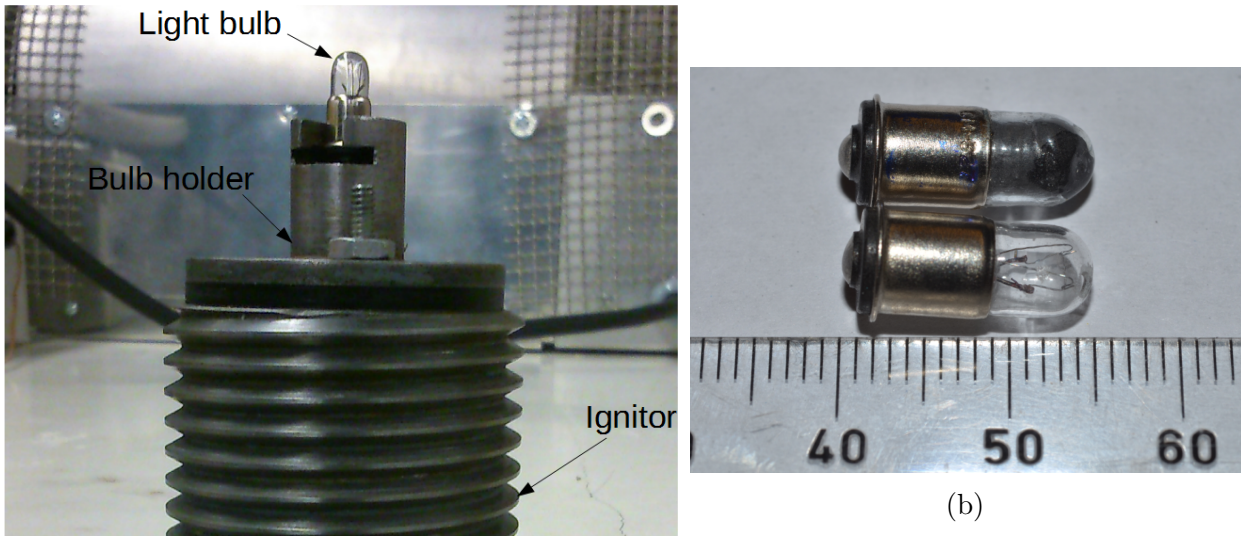

(a) (b)

Figure 2.4: Picture of a light bulb inside the bulb holder and ignitor, Figure 2.4a, and a closeup of the light bulbs used in Figure 2.4b.

to 450 kPa.

To prepare experiments, thermite samples were created by filling light bulbs with powder. They are 6 mm diameter incandescent (Chicago Miniature Lighting CM 327) bulbs rated to run at 28 V as shown in Figure 2.4b. Using a diamond cutter on a rotary tool, a small hole was made in the bulb. Thermite powder was loaded into the bulb through this hole. The mass of powder inside the bulb, on average 140 mg, was measured using a digital scale. When full, the light bulb was sealed with epoxy then left to cure overnight. During experiments, the bulbs are placed in a custom-built bulb holder on top of the ignitor as shown in Figure 2.4a.

The bulb filament generates heat when powered, starting the thermite reaction. The light bulb is broken by the reaction allowing thermite powder to spread inside the blast chamber. In preliminary tests with cells, it was found that the thermite powder was harmful to cells. In order to contain the powder and allow pressure pulse transmission, two methods of controlling the powder have been created. The first is to place a latex barrier (Bertech Black Dissipative) 0.016 in (0.41 mm) thick over the bulb holder, secured via hose clamp as shown in Figure 2.5a. The latex barriers are thin and flexible providing wave transmission while ensuring powder containment.

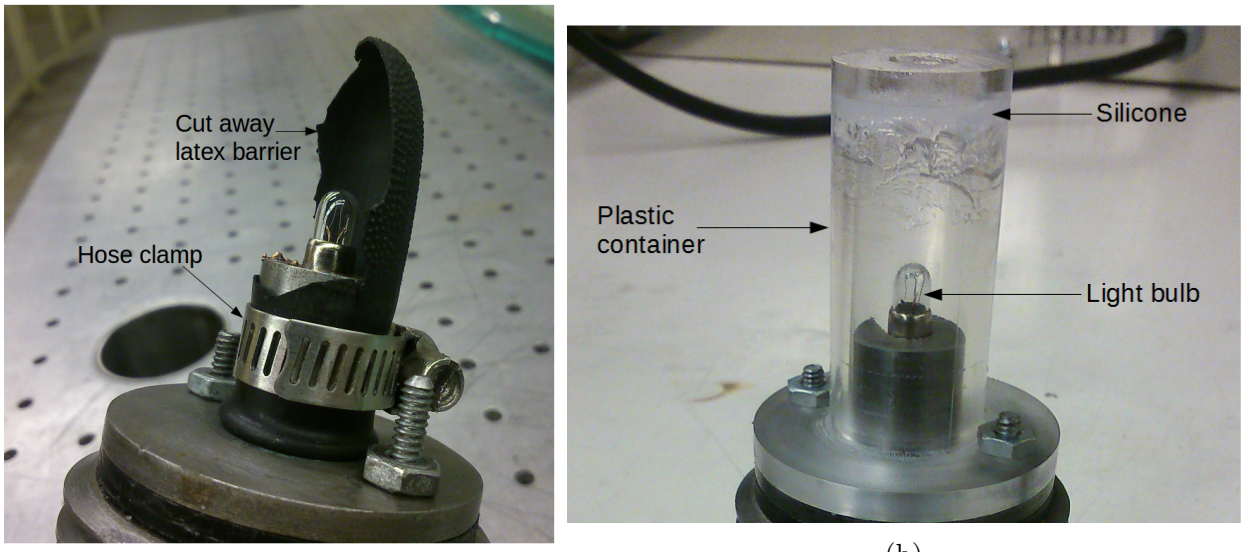

(a) (b)

Figure 2.5: Both of the thermite containment techniques. Figure 2.5a contains a picture of the latex barrier used in experiments. The barrier has been cut away to show the light bulb position position. Figure 2.5b has a picture of the silicone plug used in experiments.

The second method is using a custom silicone plug as shown in Figure 2.5b. The container's bottom has a 6 mm diameter hole sealed with a layer of silicone 14 mm thick to allow for pressure wave transmission.

2.1.3 Exploding Wire Setup

In the exploding wire technique, a thin conductive wire is rapidly heated via application of a large current. The wire breaks down into a conductive vapor that turns into plasma as current passes through it. The plasma expands which drives a shock wave into the surroundings.

The wire used in these experiments is 0.25 mm in diameter and made of tin-coated copper. It is cut to roughly 8 mm segments before soldering to the copper exploding wire ignitor leads shown in Figure 2.6.

The electrical discharge is supplied by a previously-built high-voltage ignitor (HVI) [34]. The system works by charging two parallel-plate capacitors to a desired voltage, generally between 16 KV and 24 KV, and discharging them through the exploding wire. The capacitors provide 2 μF of total capacitance. Complete discharge occurs within 100 μs and delivers 50 J of energy [34].

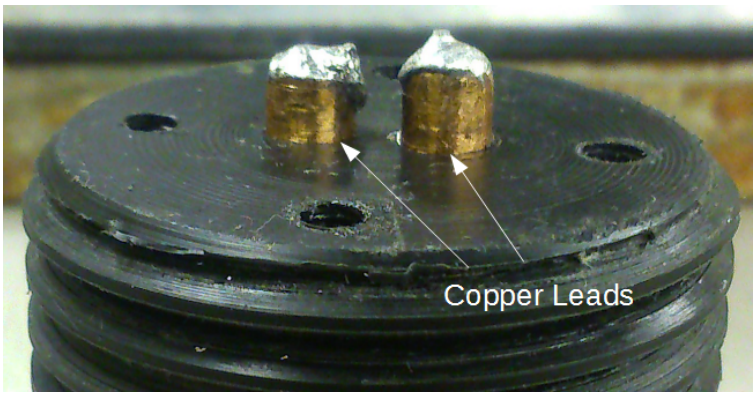

Figure 2.6: Picture of the custom-built exploding wire ignitor. The copper leads are 6.4 mm in diameter.

2.1.4 Cells Tested

As a preliminary investigation, three different kinds of *in vitro* cells were exposed to pressure waves: epidermal fibroblasts (3T3), cervical cancer epithelial (HeLa), and dog kidney epithelial (MDCK). These cell lines were selected over cells found within the skull as they are economical and have well documented behavior [35, 36, 37].

3T3 cells are laboratory grown epidermal fibroblasts originally created from mice in 1962 [38]. The green channel in Figure 2.7 designates actin filament and the red channel highlights nuclei of 3T3 cells. Fibroblasts are cells that manufacture parts of the extracellular matrix (ECM), such as collagen, which comprise most of the volume in cartilage and other connective tissues [32]. Fibroblasts also participate in healing wounds [32].

HeLa cells are cervical cancer epithelial cells first taken from Henrietta Lacks in 1951 [39]. Figure 2.8 shows a picture containing the microfilament and nuclei of HeLa. As a human cell line, HeLa has been used extensively in human epidemiology, such as polio vaccine development, and it was the first cloned human cell [39, 40]. Epithelial cells constitute the epithelium, which is a layer of tissue that coats the surfaces of organs [32]. In this tissue, epithelial cells are attached to the ECM and each other. The adhesion between neighboring cells and the surrounding matrix allows epithelial cells to transmit and support mechanical loads [32].

Madin-Darby canine kidney (MDCK) is an epithelial cell line taken from a female cocker spaniel in 1958 [41]. A photo showing the actin filament in green and red nuclei of MDCK is shown in Figure 2.9. In this image, it is clearly visible how epithelial cells group together unlike the 3T3 cells in Figure 2.7 that do not portray any grouping. The MDCK cell line has been widely used for studying epithelial cells in general, as they portray properties of more specialized cells and they can be easily grown into a monolayer [32, 42]. MDCK has been used for research on influenza and other viruses [43].

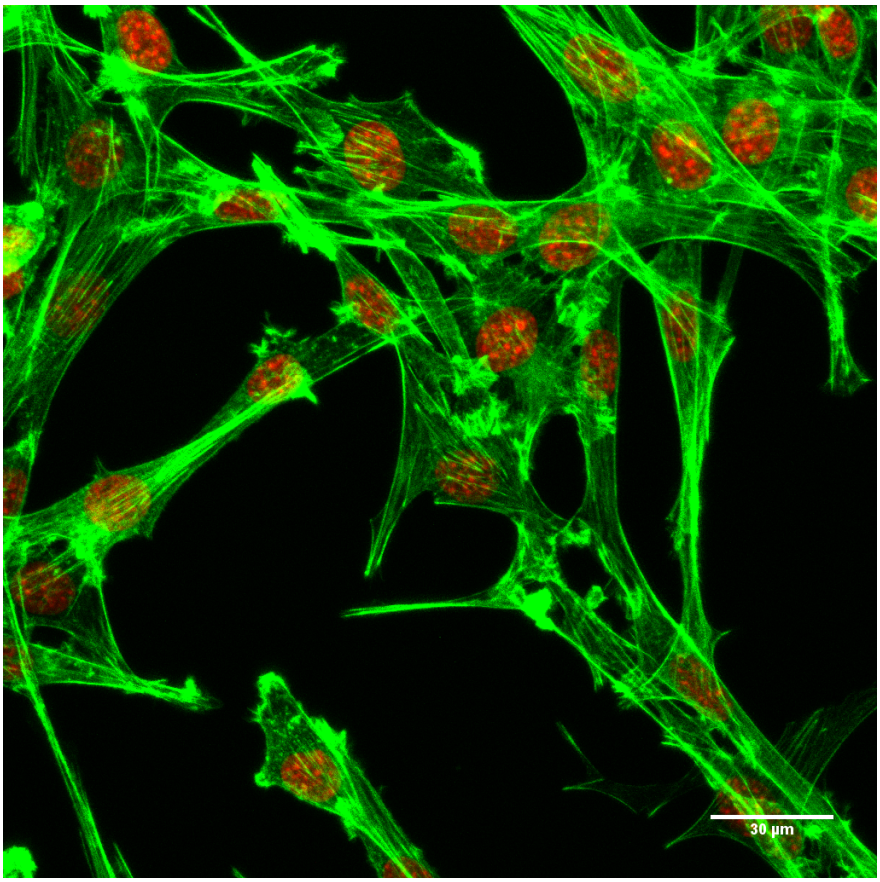

Figure 2.7: An image of healthy 3T3 cells with actin filament in green and cell nuclei in red.

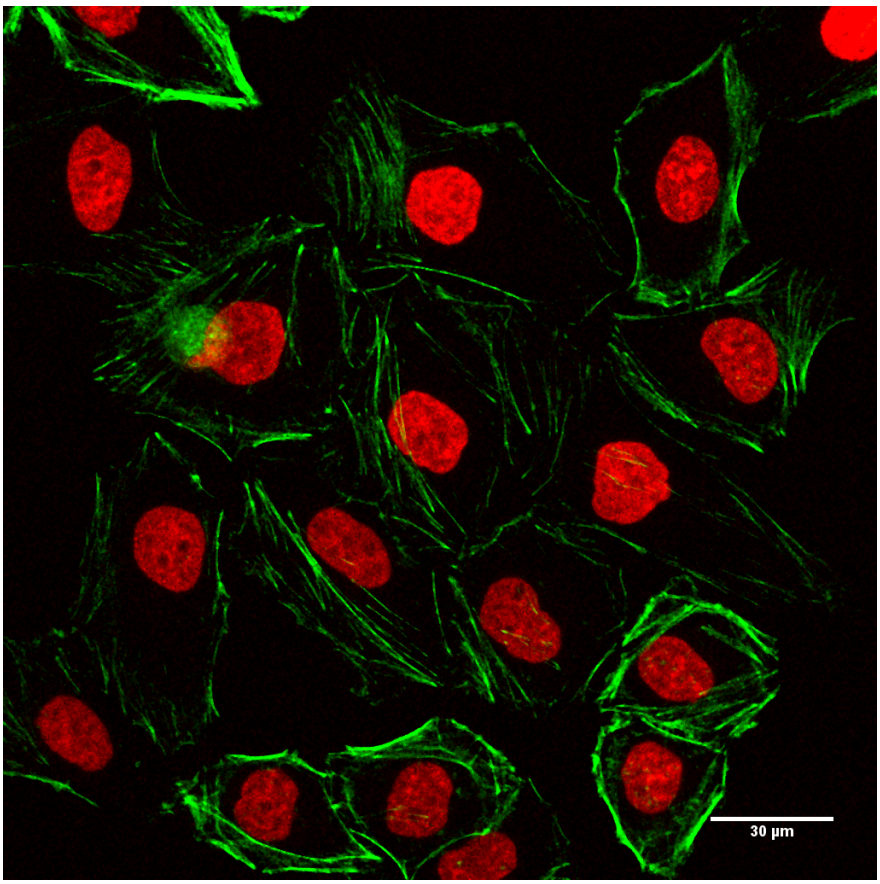

Figure 2.8: An image of healthy HeLa cells with actin filament highlighted in green and the cell nuclei in red.

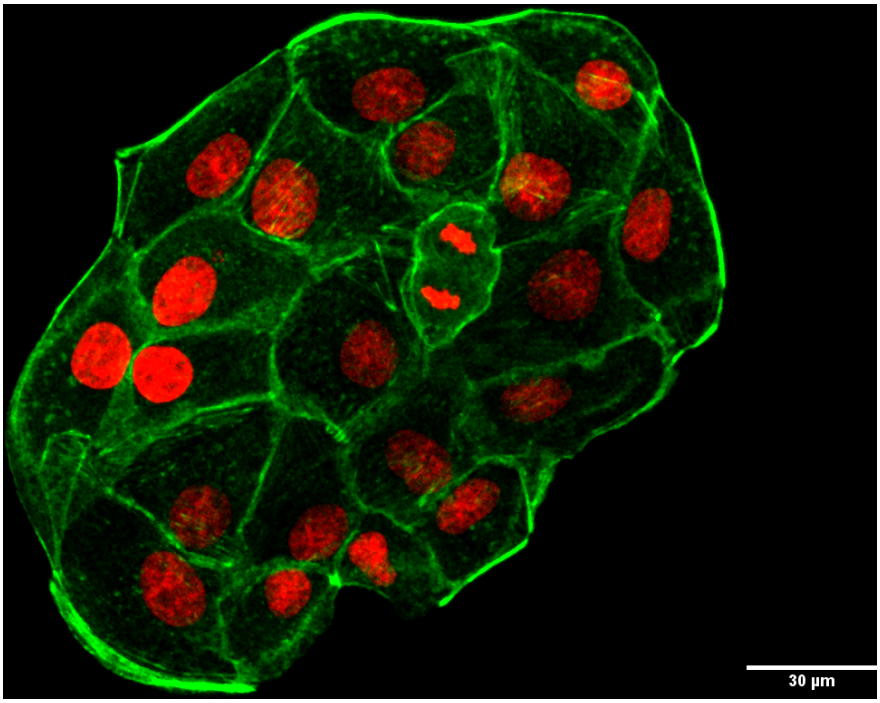

Figure 2.9: An image of healthy MDCK cells with actin filament in the green channel and the cell nuclei in red.

2.1.5 Cell Setup

Cells were grown in high glucose Dulbecco Modified Eagles Medium (DMEM) modified with 10% Fetal Bovine Serum (FBS) and 1% penicillin/streptomycin antibiotics (Hyclone). The cells were cultured at 37 °C at 5% CO_2 in 10 cm plastic plates (Fisher Scientific). The media was replaced every second day and the cells were passaged at 70% confluence. Passaging is the process of moving cells from one growth medium to another. Cells were passaged one day prior to experiments, and 25,000 were plated onto customized glass bottom 35 mm TPP cell culture dishes. A 20 mm hole was cut out of the bottom of plastic TPP 35 mm dishes with a Jamieson Laser Cutter model (LG-500) and #1.5 glass coverslips (Warner) were glued in place with polydimethylsiloxane (PDMS), which was allowed to cure at room temperature overnight. Modified TPP were sterilized with exposure to UV-light via UV-cross linker (Spectroline Select Series). All experiments were carried out in HEPES-buffered physiological saline solution (HBSS) mixed as shown in Table 2.2.

2.2 Procedure

2.2.1 Cell Experiment Procedure

Experiments testing cells were performed inside the underwater blast chamber. The cells tested are sensitive to temperature conditions and will die at room temperature. To ensure

Table 2.2: Recipe per litre of HBSS

Ingredient	Stock Concentration	Final Quantity per L
Glucose	pure	2003.33 g
HEPES at 7.4 pH	1 M	20 mL
NaCl	4 M	30 mL
$MgSO_4$	1 M	0.8 mL
KCl	2 M	2.65 mL
$CaCl_2$	1 M	1.8 mL
H_2O	pure	944.75 mL

nearly constant temperature conditions of 37 °C both the chamber and HBSS are heated prior to use. The chamber is kept in an oven overnight before testing at 37 °C while the HBSS is warmed in a water bath hours before testing.

The prepared petri dishes are loaded into the blast chamber. They are adhered to the bottom surface with vacuum grease. Up to four dishes were tested simultaneously by placing them in the four corners of the blast chamber as shown in Figure 2.10. After the device is bolted closed, HBSS is slowly added to the chamber using a funnel. The containment method, either latex barrier or silicone plug, is then filled with distilled water and attached to the ignitor. When the chamber is full of HBSS the ignitor is inserted.

The power supply is then connected and the thermite is ignited. The used HBSS is drained from the chamber and petri dishes removed. Multiple petri dishes, up to four, were used for each thermite sample. For each experiment one dish is used to study the immediate effect of the pressure loading. Cells in the remaining dishes are allowed to recover for a set period of time.

In order to stop cell recovery, dishes are fixed with 3.5% paraformaldehyde and permeabilized with Triton X-100 at 37 °C. Staining for microfilament was performed using Phalloidin Alexa Fluor 546 (Invitrogen). DNA was marked with DAPI (Invitrogen) stain, also on ice. Finally, imaging was performed using a Nikon A1R high speed laser scanning confocal system on a TiE inverted optical microscope platform (Nikon Canada).

2.2.2 Pressure Measurement

For experiments measuring pressure loading on cells, the wall mounted sensor was placed on the bottom surface of the blast chamber. In these tests no petri dishes were inside the chamber, however the latex barrier or silicone plug was still used. In exploding wire tests no containment technique was used. The freefield pressure sensor was employed for these tests to measure shock pressure.

The procedure to obtain pressure data from thermite reactions is as follows. With the wall sensor at the chamber's bottom surface, the device is filled with water. The loaded thermite sample is then placed in the ignitor. Next either a latex barrier or silicone plug is fitted onto

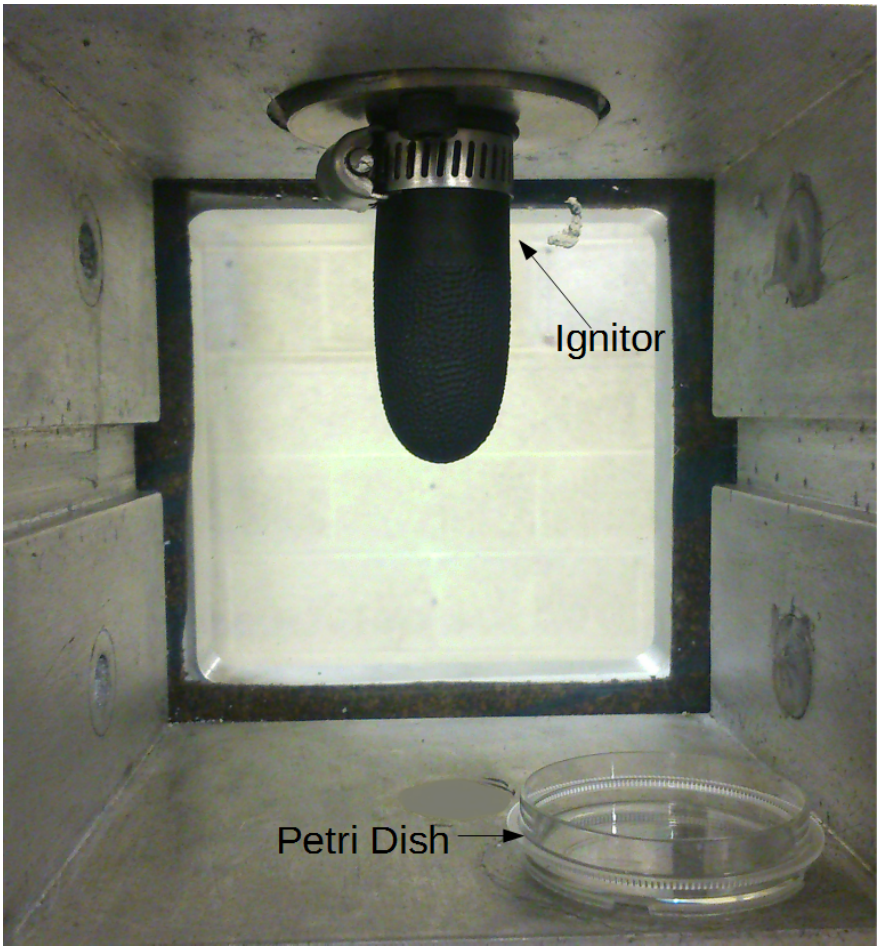

Figure 2.10: Picture of inside the blast chamber showing the position of a petri dish for cell experiments.

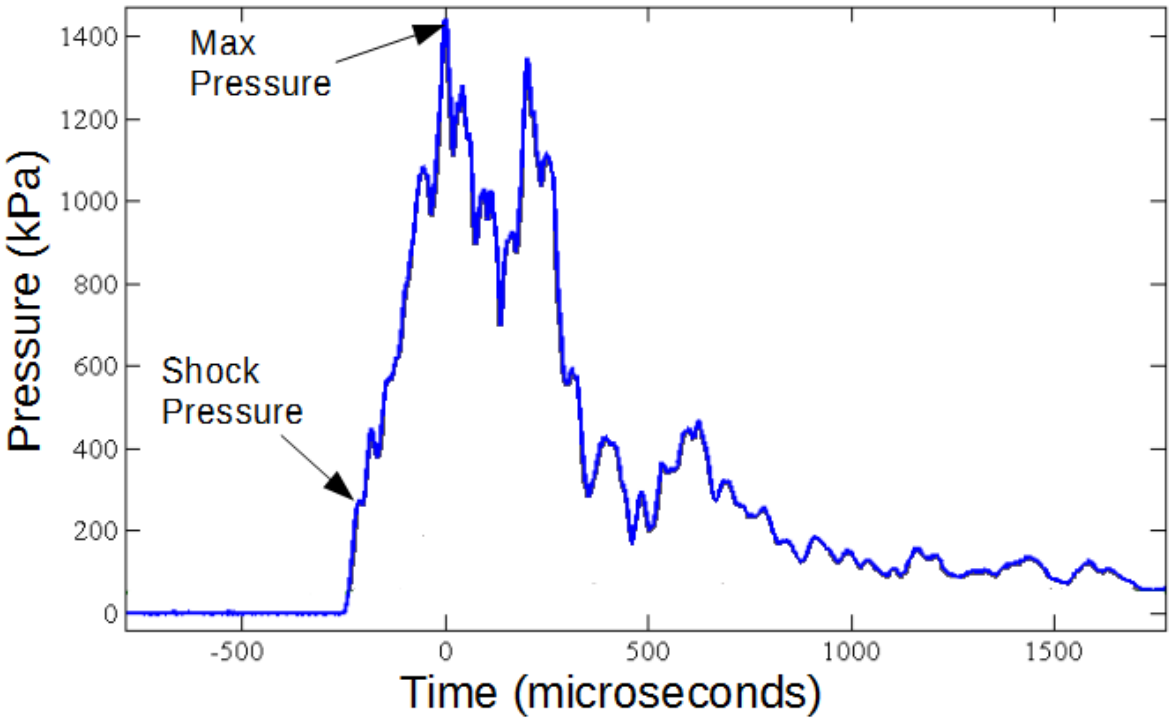

Figure 2.11: Pressure vs time plot typical of thermite experiments with key pressure signature features highlighted.

the ignitor. The ignitor is screwed into the blast chamber. Finally the thermite is ignited and pressure data recorded.

The procedure to obtain pressure data from exploding wire experiments is very similar to the thermite experiments. First, the freefield sensor is placed inside the chamber a set distance from the bottom wall. In all tests the sensor was 47.5 mm from the bottom wall. Next, the chamber is filled with distilled water. After soldering the exploding wire to the leads, the ignitor plug is inserted into the chamber. The HVI is then connected to the ignitor and charged to a desired voltage. The HVI is finally discharged and pressure data obtained. The acquired data is analyzed the same way as thermite experiment data. A typical pressure profile for thermite experiments is shown in Figure 2.11 where the first quick rise in pressure was recorded as the shock pressure and the maximum pressure was set at time equals zero.

2.2.3 Post-Processing

In order to eliminate ringing, collected data from thermite experiments was post-processed using an equiripple low-pass filter built into MATLAB with filtering parameters detailed in Table 2.3. Signals above the resonant frequency of the pressure sensor were blocked. The wall-mounted sensor had a known resonant frequency of 500 kHz. The effect filtering has on data from the wall-mounted sensor is presented in Figure 2.12. The code used to filter this data is in Appendix B.

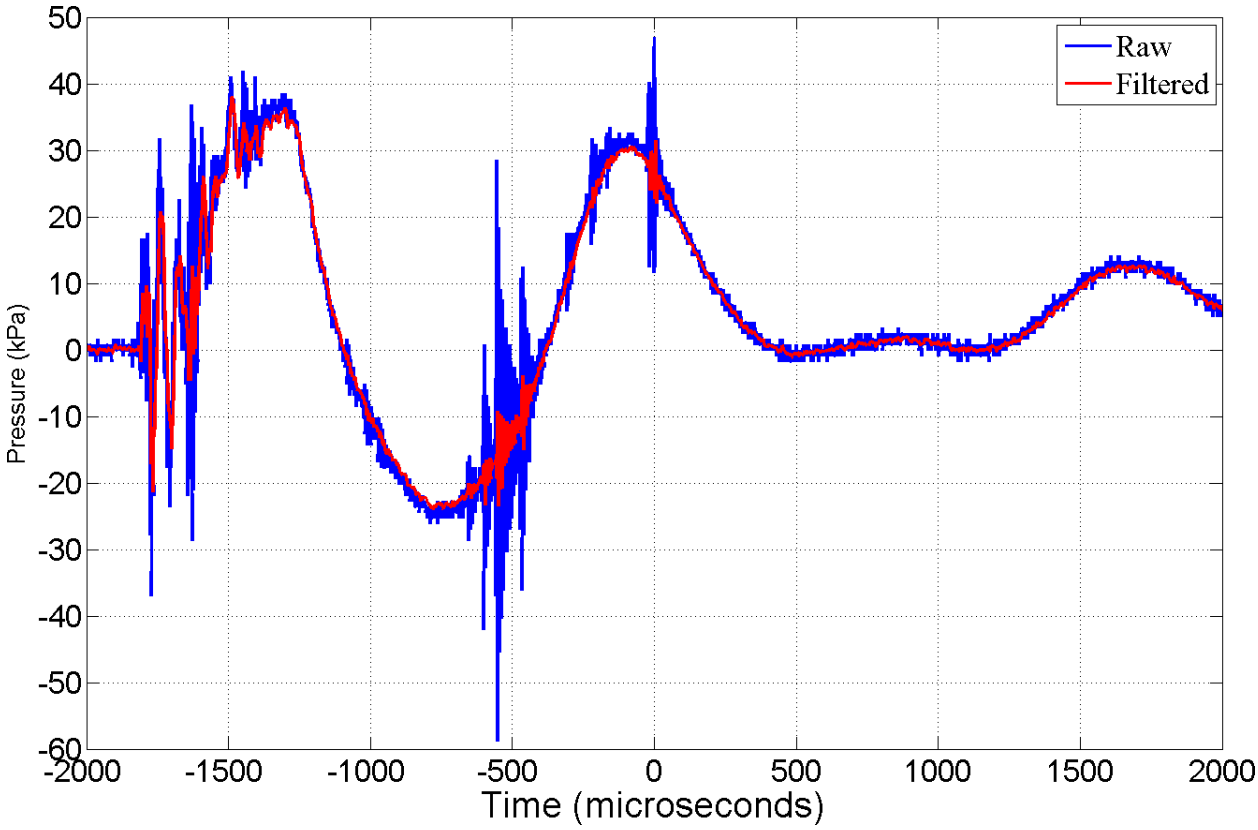

Figure 2.12: Comparison of pressure vs time plots for raw and filtered data.

Table 2.3: Table of low-pass filter parameters

Filter Parameter	Wall-Sensor	Freefield Sensor
Pass-Band Ripple (dB)	1	1
Stop-Band Attenuation (dB)	60	60
Pass-Band Start (kHz)	$1 \cdot 10^{-4}$	$1 \cdot 10^{-4}$
Pass-Band End (kHz)	500	200
Sampling Rate (kHz)	1000	250

The blue curve shows the raw data with significant ringing at -500 μs and again near 0 μs. The red curve is the filtered data which greatly reduces noise in the pressure signal. After 0 μs high frequency ringing is dampened by the filter without much deviation from behavior in the raw data.

The resonant frequency of the freefield sensor was not specified by the manufacturer. In order to determine the natural frequency, a sample of ringing when the sensor was open to ambient conditions was taken. The fast-Fourier transform (FFT) was performed in MATLAB to determine frequency content of the sample. The natural frequency of the sensor was found to be 200 kHz. The data produced by this sensor was passed through a low-pass filter written in MATLAB with parameters defined in Table 2.3. The code used in the FFT analysis is in Appendix B.

In order to detect the presence of a shock wave in the filtered pressure signal, it is of interest to measure the response characteristics of the filter used. It can be shown underwater shock waves of 1.7 MPa strength have a rise time on the order of nanoseconds [44]. A unit step function was used in order to approximate an underwater shock wave. The function was passed through both of the filters defined in Table 2.3. The filtered unit step is presented in Figure 2.13.

The blue line in Figure 2.13 shows the unit step behavior that changes from 0 to 1 at time equal to zero. The green curve shows how the 500 kHz low-pass filter has smoothed the unit step transition. When time is between -1 and 9 the green curve is increasing, defining a rise time of 10 μs for the 500 kHz low-pass filter. The red curve shows the 200 kHz low-pass filter response which has further smoothed the unit step behavior. The red curve begins to rise at -4 microseconds and continues until 20 microseconds. For this filter the rise time was 24 μs. For pressure data obtained with the wall-sensor processed with the 500 kHz low-pass filter, signals changing on the order of 10 μs or faster may be related to shock waves. For data from the freefield sensor and passing through the 200 kHz low-pass filter, shock waves may be associated with signal variations on the order of 24 μs or faster. Pressure variations that occur much slower than 10 μs and 24 μs respectively are not related to a shock wave.

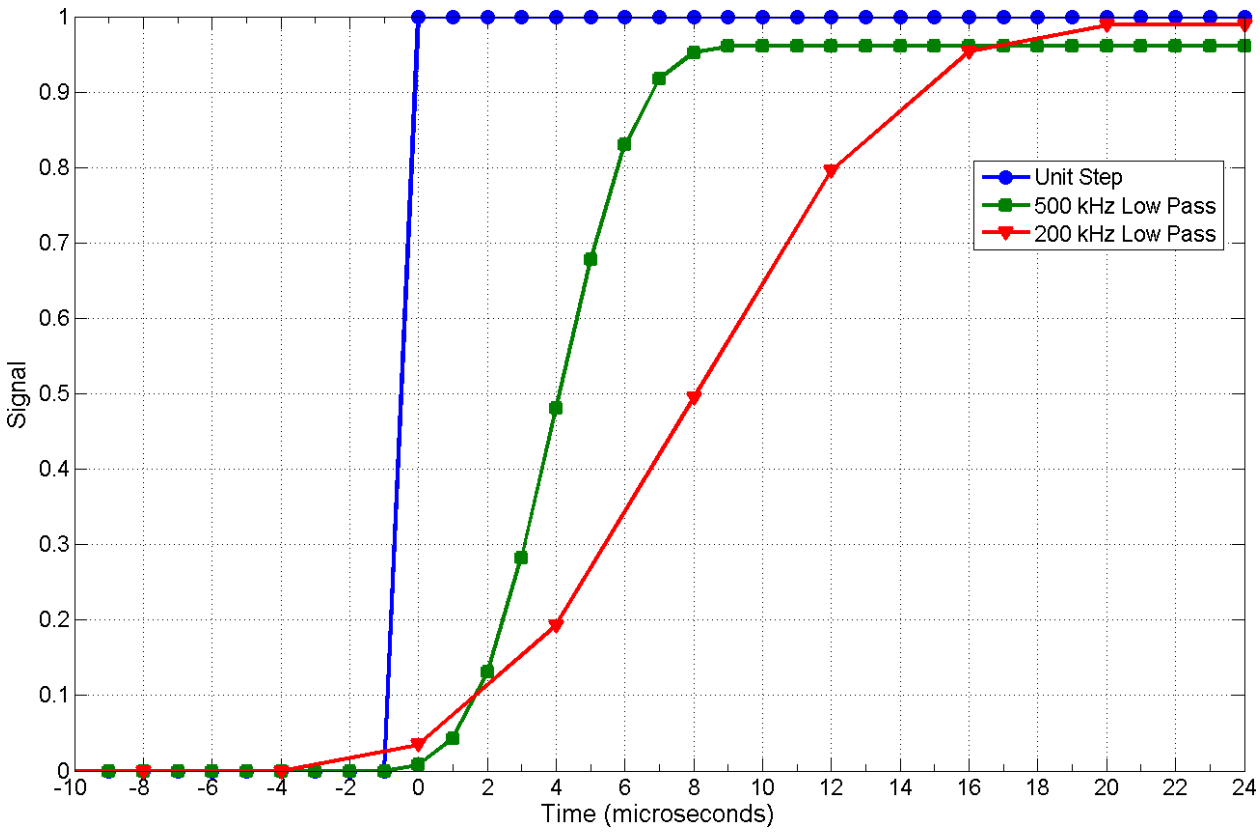

Figure 2.13: Plot of signal vs time for a unit step function before and after filtering.

Chapter 3

Results

In this chapter, first the pressure waves generated by thermite reaction and exploding wire are characterized. The affect thermite generated pressure waves have on 3T3, HeLa, and MDCK cells is then presented.

3.1 Pressure Wave Characteristics

Cells were not exposed to pressure waves in experiments where pressure data was obtained. Pressure data collection was performed to measure the loading cells experience. Figure 3.1 plots pressure against time for the bottom wall sensor in an experiment using the silicone plug with unmilled powder. For all graphs presented, the maximum pressure is aligned with time set to zero. In Figure 3.1, the pressure amplitude is below 40 kPa at all times. The two 1 millisecond period waves have clearly visible ringing associated with acoustic wave dynamics. The waves with a period of about 1 millisecond are likely related to resonance of the silicone plug. It takes about 750 μs for the pressure to rise to around 40 kPa. The maximum pressure occurs near the peak of the next large crest, over 1000 μs after the first crest. The pressure evolution generated by reacting unmilled thermite inside the silicone plug will represent the smallest loading tested in cell experiments.

Figure 3.2 and 3.3 contain pressure profiles produced using a latex barrier as the containment method for unmilled and milled thermite reactions. First is the unmilled thermite experiment shown in Figure 3.2 where pressure is measured using the wall-mounted sensor. Immediately visible in this plot is the increased pressure magnitude of just under 700 kPa before decreasing to a second peak near 250 kPa. The pressure rises at around -300 μs and by 1000 μs the pressure has dropped below 50 kPa. It takes 300 μs for the pressure to reach a clear peak at zero microseconds. 300 μs is much larger than the 10 μs filter rise time; therefore, there is no pressure jump associated with a shock wave. Unmilled aluminum copper(II)-oxide thermite powder is known to have a low reaction rate. This has been shown to be related to underwater shock strength where a low reaction rate correlates to a weak pressure wave [31].

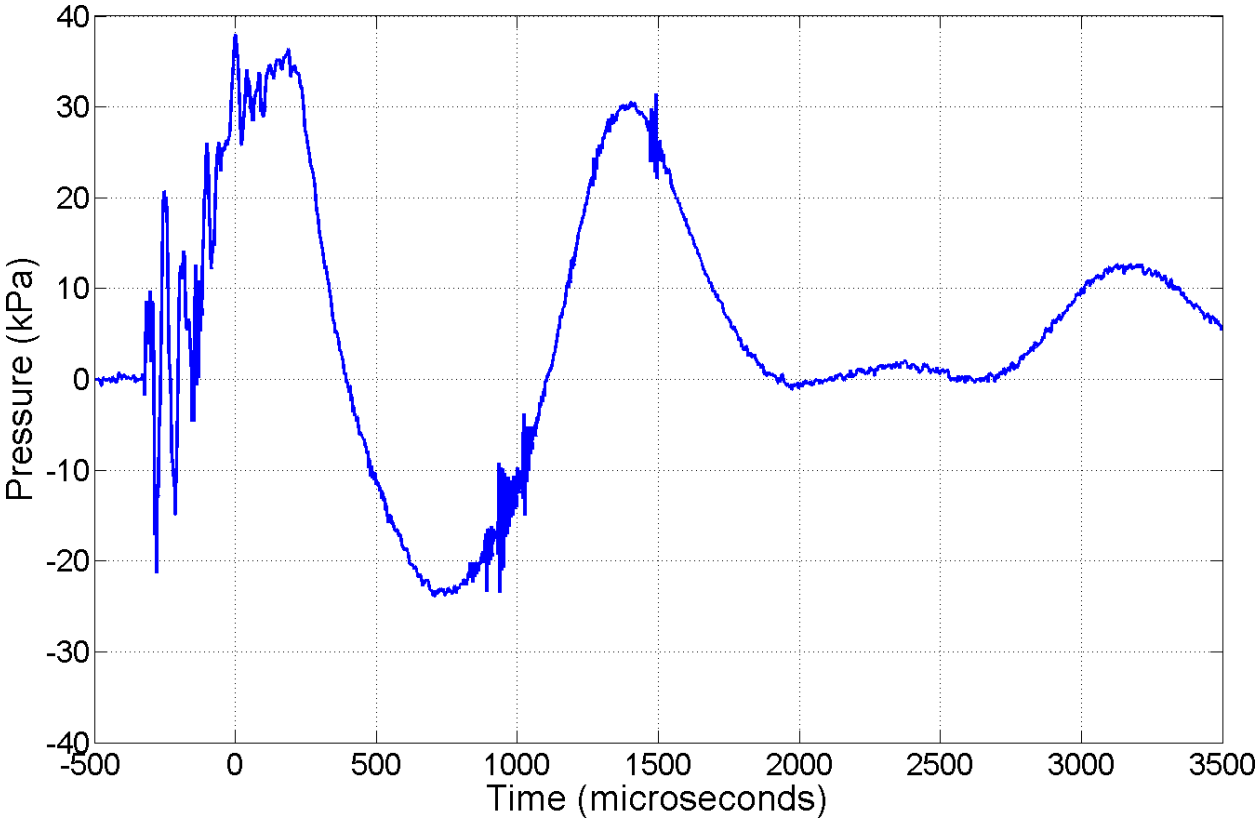

Figure 3.1: Pressure vs time plot produced from unmilled thermite reacting in the silicone plug. In this test the wall-sensor was used.

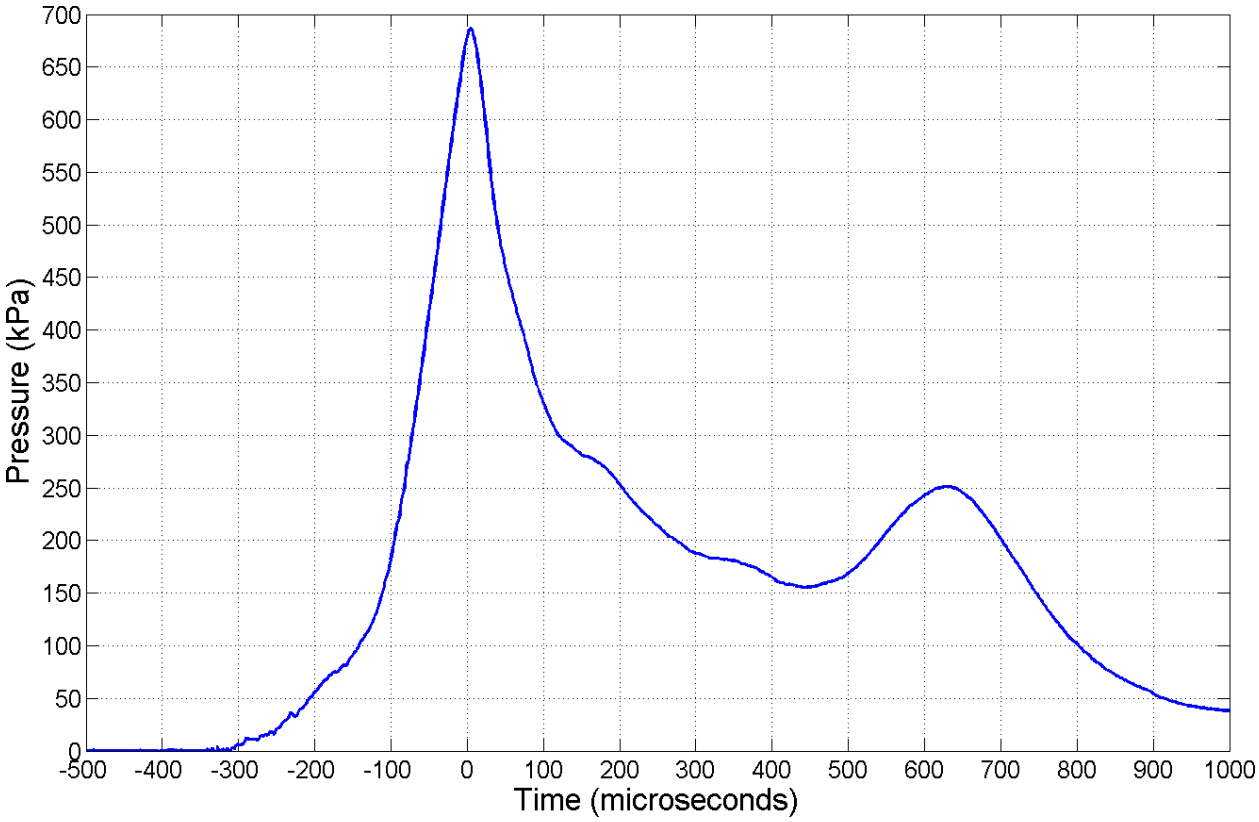

Figure 3.2: Pressure vs time plot produced from unmilled thermite reacting inside a latex barrier. In this test the wall-sensor was used.

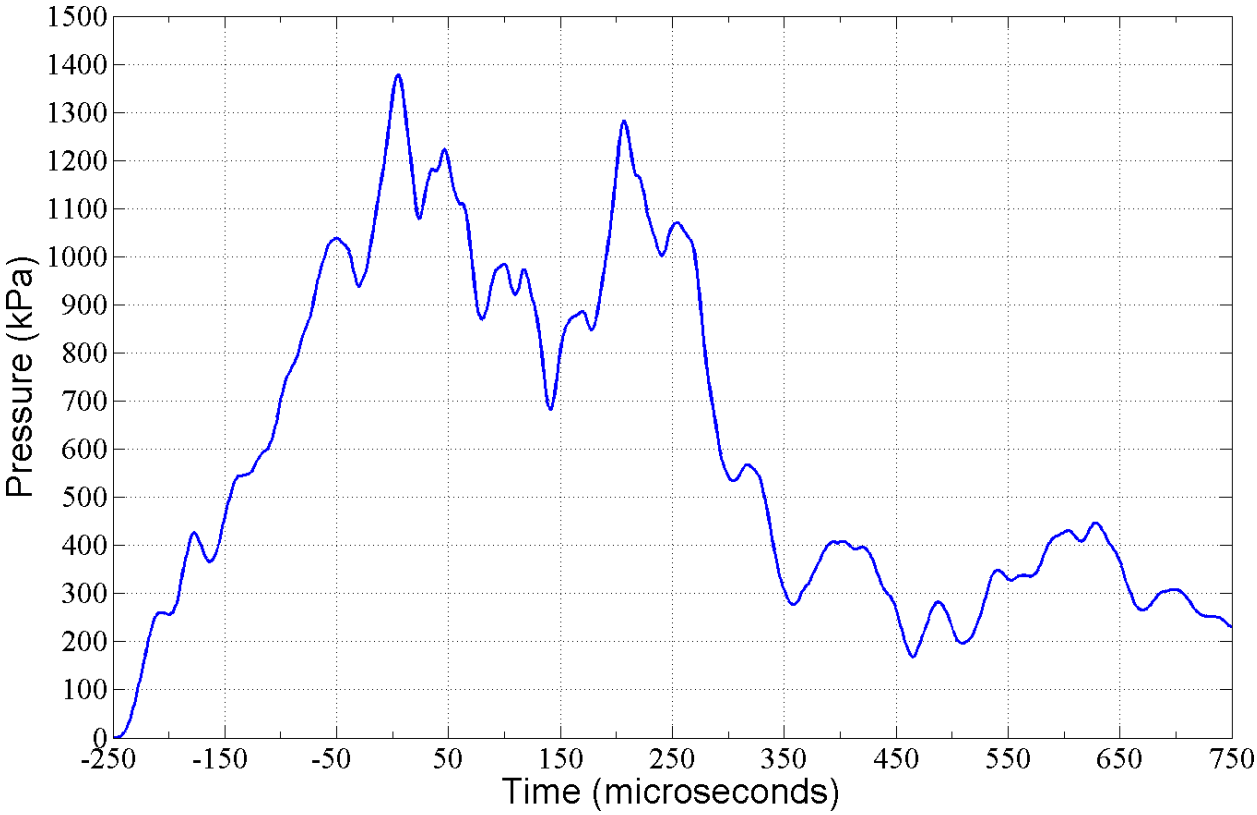

Figure 3.3: Pressure vs time plot produced from milled thermite reacting inside a latex barrier. In this test the wall-sensor was used.

Figure 3.3 shows the pressure evolution created by milled thermite reacting inside the latex barrier. The pressure field was captured using the wall-mounted pressure sensor. The pressure range has increased, this time to a maximum of near 1400 kPa. Between -250 μs and -200 μs the pressure jumps from zero to just under 300 kPa. This pressure rise occurs in about 40 μs. This time difference is on the same order of magnitude as the filter rise time, 10 μs. This means the pressure rise to near 300 kPa suggests the presence of shock wave. Around 200 μs after the maximum pressure a second peak near 1300 kPa is visible. The milled thermite has a much higher reaction rate than unmilled powder which allows it to drive a stronger pressure wave underwater.

The pressure evolution produced from exploding wire experiments collected with the freefield sensor is presented in Figure 3.4. The negative reading just after -50 μs is electrical noise produced by the HVI discharge. The first peak at over 5 MPa occurs about 15 μs after the pressures reads zero. This rise time is smaller than the 24 μs filter rise time. It is likely a shock wave creating the maximum pressure above 5 MPa. This is followed by two more peaks just under 5 MPa. After the third peak, the pressure drops off towards 500 kPa by 450 μs.

Table 3.1 summarizes the key pressure evolution characteristics for the tested experiments. It was found that the silicone plug significantly lowers maximum pressure to 40 kPa compared to the latex barrier at 430 kPa. In both of these setups no clear shock wave was detected.

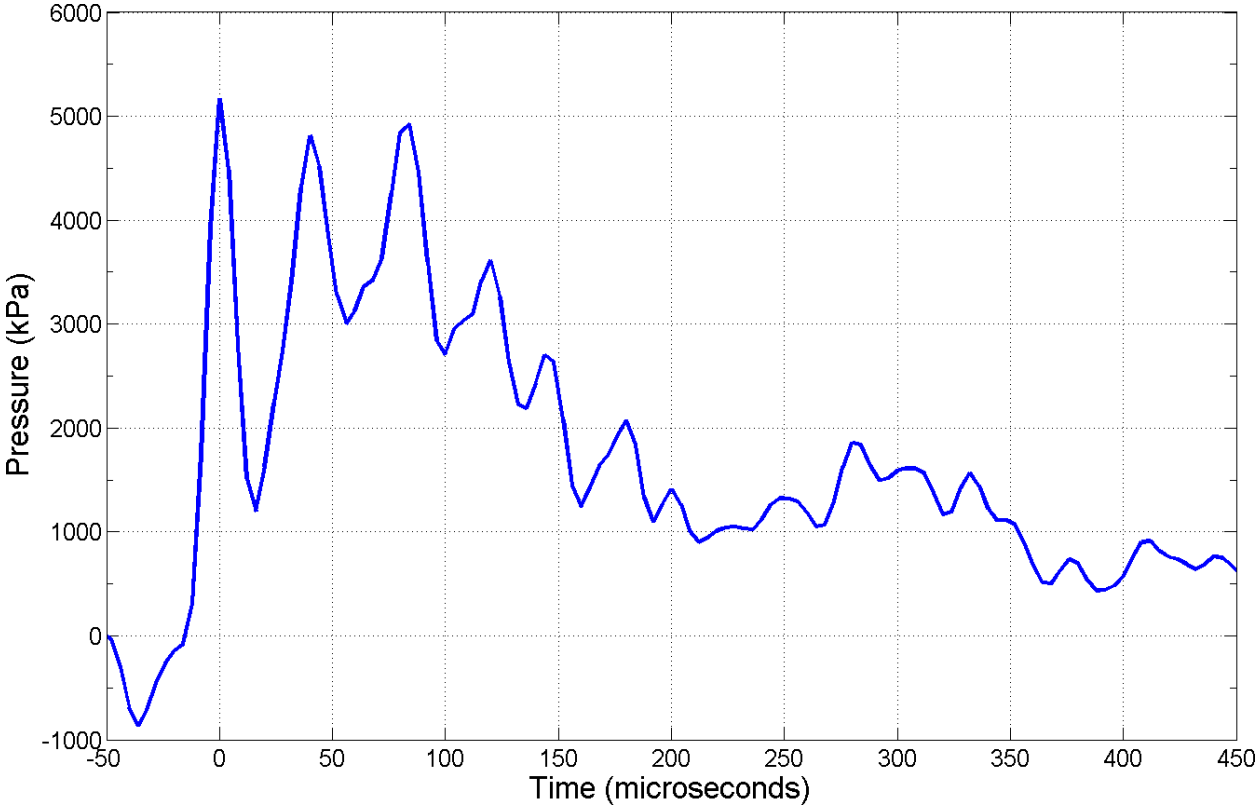

Figure 3.4: Pressure vs time plot created by an exploding wire test. This was recorded using the freefield sensor.

Table 3.1: Summary of shock and peak pressures for thermite and exploding wire experiments.

Conditions	$P_{shock}\pm$ SE (kPa)	$P_{max}\pm$ SE (kPa)
Unmilled Thermite Silicone Plug	no shock	40 ± 6
Unmilled Thermite Latex Barrier	no shock	430 ± 90
Milled Thermite Latex Barrier	300 ± 20	1500 ± 100
Exploding Wire	4200 ± 100	4500 ± 200

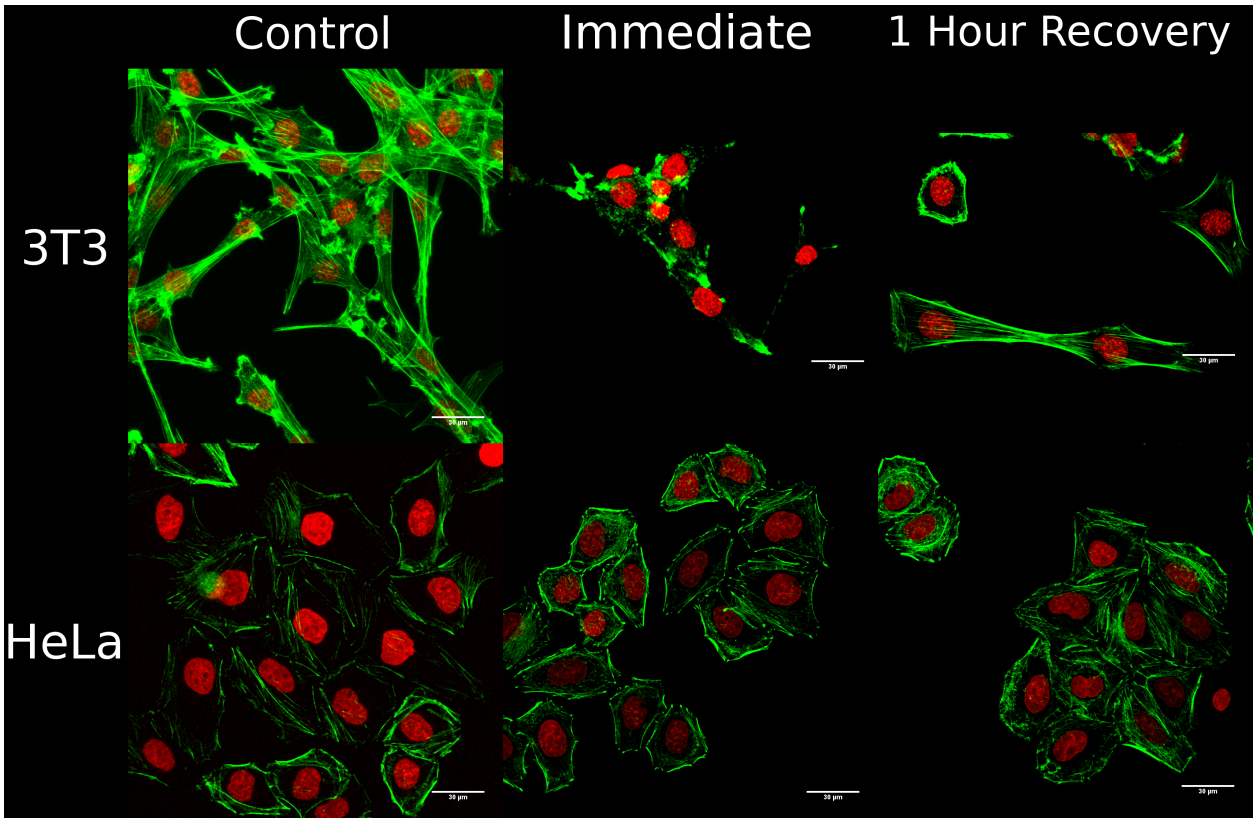

Figure 3.5: Images of tested cells before and after exposure from pressure waves generated by reacting unmilled thermite inside the silicone plug.

Utilizing milled powder created a discernible shock wave with a 300 kPa pressure. This led to the peak pressure being 1500 kPa. The exploding wire drove the strongest shock wave at 4200 kPa shock pressure followed by 4500 kPa maximum pressure.

3.2 Actin Modification

In each experiment, multiple petri dishes were exposed to pressure waves. Results are presented from two dishes. One dish was used to measure the immediate cellular response. Cells in the other dish were allowed to recover for one hour before their response was evaluated. Results are presented by looking at the immediate response first and the one hour recovery condition second. Control images presented are from cells that experienced all of the same conditions as tested cells except shock wave exposure. This eliminates factors such as vibrations produced from opening and closing the chamber. In all images, the green channel displays actin filament while red identifies cell nuclei

3T3 and HeLa cells were tested to measure their response to pressure waves produced from reacting unmilled thermite using the silicone plug. The left most column of Figure 3.5 shows images from a control experiments detailing the microfilament network in healthy

cells. Variations in color intensity within the nucleus are caused by different concentrations of nuclear material.

The first row of Figure 3.5 contains images of 3T3 cells immediately after exposure and following 1 hour recovery. Immediately after exposure collapsed microfilament is visible throughout the image in the second column indicated by the short green regions. After the 60 minute recovery period, the collapsed filament has reverted to its original form which is similar to the control image. The nuclei showed no major change in morphology at all times.

The second row of Figure 3.5 shows how HeLa cells respond to these pressure waves. The first column shows a control image of HeLa cells. The immediate response of these cells, displayed in the second column, shows no major actin filament collapse. The nuclei, highlighted in red, look to have retained their original shape when compared with the control image. Cells in the other petri dish were allowed to recover for one hour before being imaged as shown in the third column. Both the cell nuclei and microfilament do not appear to have changed morphology compared to the control.

Continuing to use unmilled powder but using a latex barrier instead of the silicone plug was shown to increase the maximum pressure from ∼40 kPa to ∼430 kPa. Figure 3.6 contains images of the cellular response of 3T3, HeLa, and MDCK cells to these pressure waves.

The image in the first row and second column of Figure 3.6 shows the immediate response of the 3T3 cells. The nuclei appear to have the same shape as those in the control image. The green channel shows collapsed actin microfilament indicated by the change in structure compared to the control. The image in the third column shows that when allowed to recover for 1 hour, the microfilament has regained a form similar to the control. In this image the cell nuclei are faint and hard to see clearly.

Results for the response of HeLa cells are in the second row of Figure 3.6. In the second column, the cell nuclei pictured immediately after exposure do not appear deformed compared to the control image. Similarly, the actin filament appears to have retained its original morphology as there are no clear areas of collapse. After a one hour recovery period, there is no visible collapsed filament. In addition, the shape of the nuclei appears unchanged compared to the control.

The third row of Figure 3.6 contains images of MDCK cells. In the left most column a control image of these cells is presented. Immediately after pressure wave exposure, the nucleus morphology in the second column appears the same as in the control. There does not appear to be any indication of microfilament collapse in this image. The image in right most column shows the status of cells in a separate petri dish when allowed to recover for one hour. The cell nuclei have comparable morphology to the control. The actin filament appears shows no collapse, making it similar to the image taken immediately after exposure.

Milled thermite, characterized by a 300 kPa shock pressure and 1500 kPa maximum pressure, was used next. A latex barrier was employed as the containment technique for this test. Figure 3.7 displays images of 3T3, HeLa, and MDCK cells response to this pressure field.

The first row of Figure 3.7 contains 3T3 cells. In the second column, the cell nuclei show no major difference in shape when compared to the control image. There are several regions of

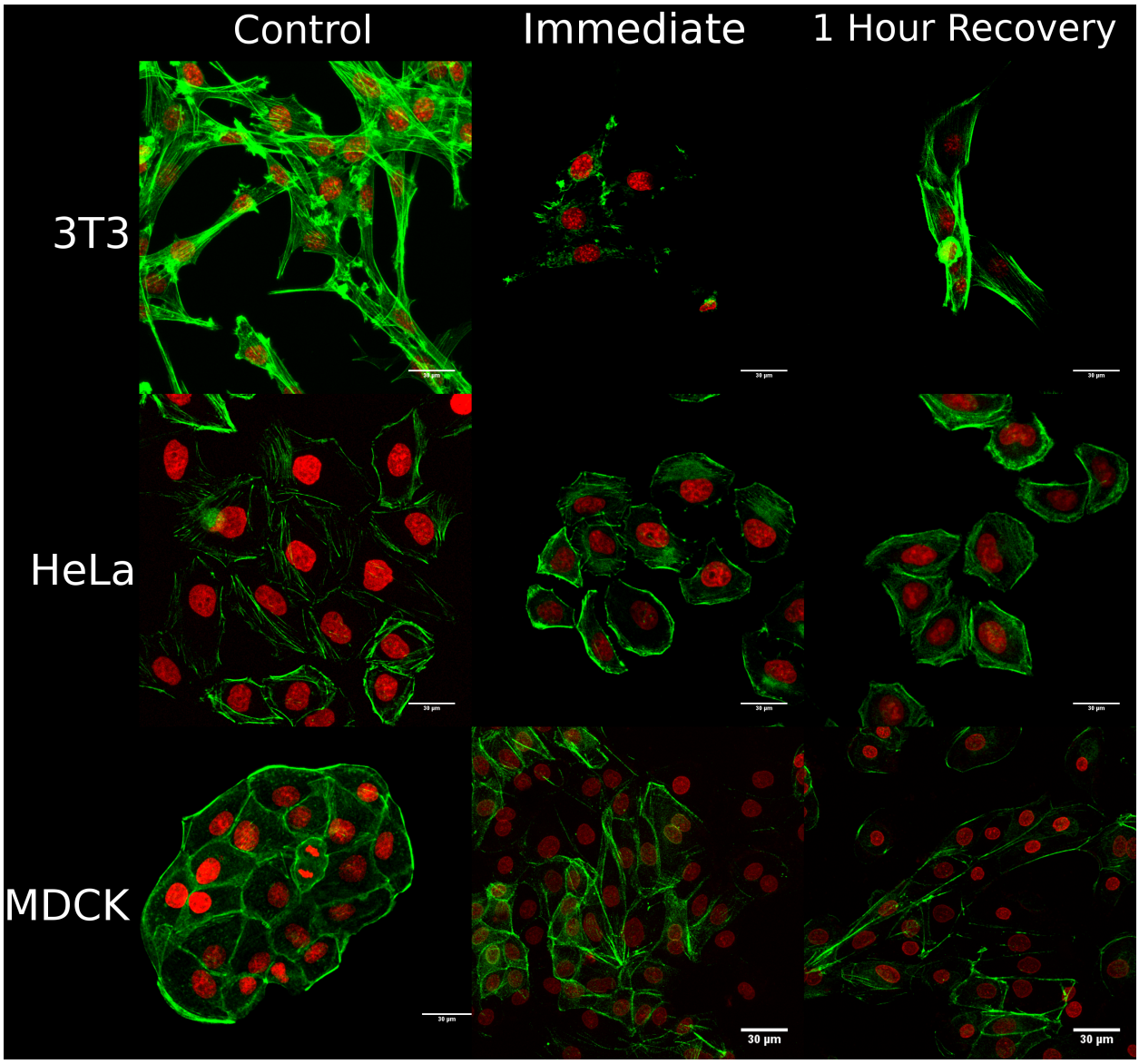

Figure 3.6: Images of tested cells before and after exposure from pressure waves generated by reacting unmilled thermite inside the latex barrier.

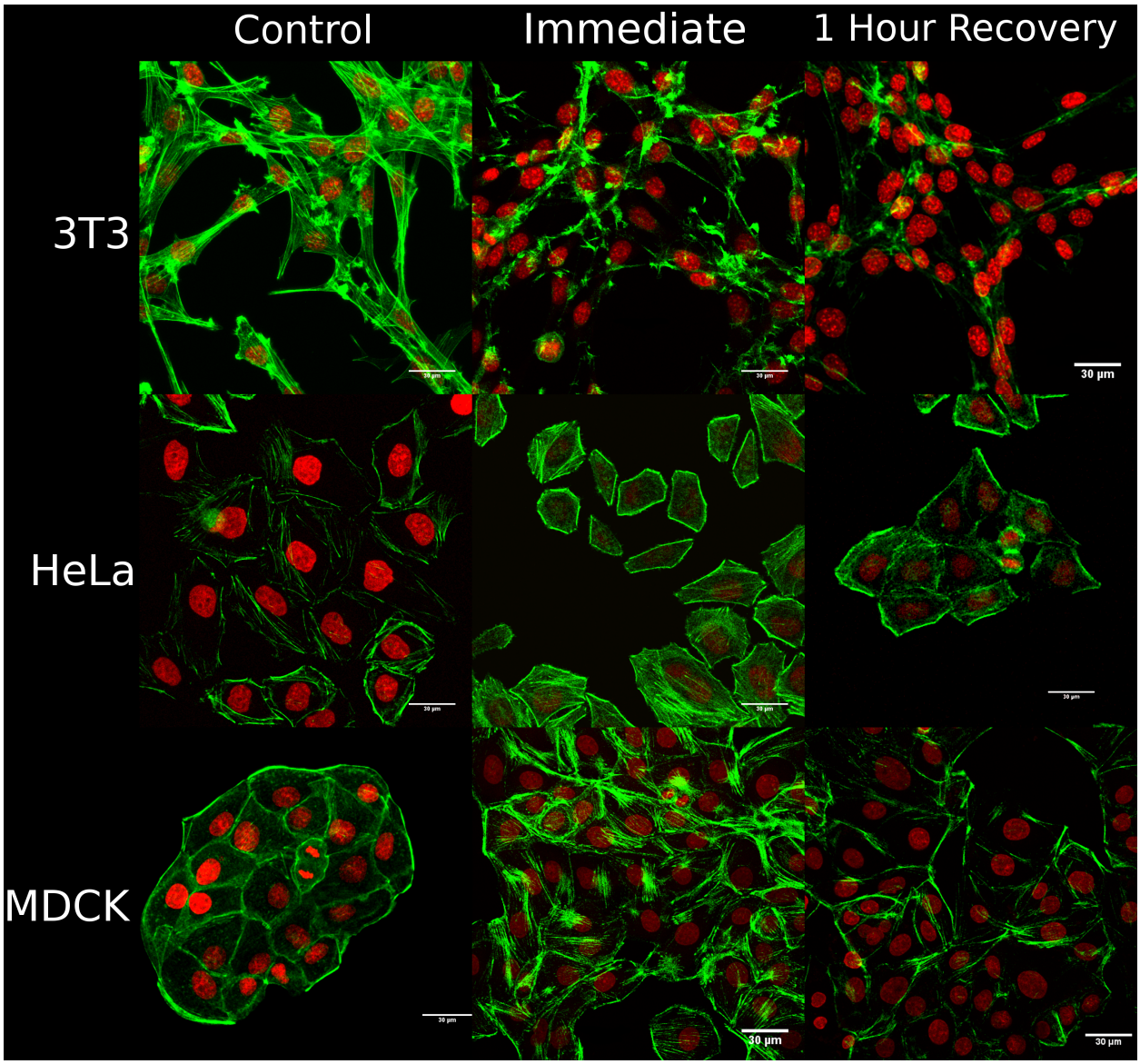

Figure 3.7: Images of tested cells before and after exposure from pressure waves generated by reacting milled thermite inside the latex barrier.

collapsed actin filament present in this image. In the third column, the 3T3 cell state after recovery is shown. The microfilament appears to have reverted from its collapsed structure. The nuclei appear to be in the same condition as the control image.

The next row in Figure 3.7 features HeLa cells. The image in the second column displays the response of HeLa cells immediately after being exposed. The microfilament in the green channel does not appear to have collapsed while the cell nucleus shape has not changed. After the HeLa cells in a different dish were allowed to recover, an image was taken shown in the third column. The nuclei appear to be much like the control image, indicating no major change in shape. The microfilament also shows no significant deviation from the picture immediately after exposure and appears similar to the control image.

The response of MDCK cells to the shock wave driven by reacting milled thermite is presented in the bottom row of Figure 3.7. There is no microfilament collapse visible immediately after wave exposure as shown in the second column. Morphologically, there does not appear to be any difference between cell nuclei in this image and in the control image. Cells exposed to the shock wave from milled thermite were given one hour to recover before being imaged, as shown in third column. The actin filament structure appears similar to the immediate and control images, indicating no change in features. Moreover, no change in nuclei shape was detected.

Chapter 4

A Model For Shock Wave Induced Cell Damage

In this chapter, the results presented and potential cellular damage mechanisms are discussed. A model for predicting cell modification based on shock strength is established and discussed. The model compares shock thickness to cell size in order to anticipate damage. The estimates of shock thickness in water use the method outlined by Thompson and a modified Tait/stiffened gas equation of state. This describes the compressibility of water in the range of pressures relevant to TBI [45]. A derivation for the shock jump relations in water utilizing the stiffened gas equation of state is summarized with a full derivation in Appendix A. The model predictions are then compared to experimental results.

4.1 Discussion

Three different cell lines, 3T3, HeLa, and MDCK were exposed to the shock waves produced from reacting thermite. Immediately after the explosion, cells were imaged in order to detect changes in actin filament structure. In a separate petri dish exposed to the same explosion, cells were allowed to recover for one hour before having pictures taken.

It was found that the microfilament in 3T3 cells is collapsed when exposed to a pressure wave created from both a milled and unmilled thermite reaction. The same response was also found using both the silicone plug and latex barrier to trap thermite powder. This result suggests that regardless of thermite containment technique, 3T3 cells' actin filament appears to respond the same way. 3T3 cells were found to be sensitive to disturbances in their environment, evidenced by the collapse of actin filament in response to minimal loading conditions, $\sim$40 kPa peak pressure waves. When allowed to recover, the microfilament reverted to its original form. In all 3T3 tests, the cell nuclei shape did not noticeably change.

HeLa cells showed no collapse of actin filament in both milled and unmilled thermite tests. As with the 3T3 cells, it appears the thermite containment technique had no effect on the

resulting change in microfilament structure. The cell nuclei of HeLa were not found to change shape after shock wave exposure.

The actin filament in MDCK cells was found to remain as filament in response to the loading produced from both unmilled and milled thermite. This is similar to the durability shown by HeLa's microfilament. MDCK's cell nuclei were found to retain the same shape immediately after the explosion and following recovery.

Of the three cell lines tested, HeLa and MDCK had less sensitive actin filament than 3T3 cells. MDCK and HeLa showed no visible actin collapse. The actin filament in 3T3 cells was found to collapse in response to all pressure loading conditions tested. The difference in these results may be attributed to the different cell types tested. 3T3 is a fibroblast whereas HeLa and MDCK are epithelial cells.

It is not uncommon to see a cell type dependence on damage. It has been previously found that the brain has a shock pressure injury threshold of less than 1 MPa [18]. This is lower than the limits found in the kidneys, at 3 MPa, and lungs, at 2 MPa [46, 47]. The difference in these thresholds is likely related to the unique properties of each cell type. For a sufficiently strong shock wave, damage at both microscopic and macroscopic scales will occur. Structural changes to neurons have been found in response to 1 MPa shock waves in saline solution and 338 kPa shock waves in air [17, 18]. It has been shown that hemorrhaging from ruptured blood vessels is a macroscopic result of shock wave loading [3]. At microscopic scales however, the mechanism to produce damage is unclear.

The potential mechanisms to produce cellular damage in response to a shock wave include shock compression and dynamics within the shock wave. In compressive loading, cellular components are forced together as the whole cell volume decreases. As the cell is compressed it spreads over an increasing area while reducing its thickness. The change in cell thickness would be small for a weak shock wave and no cell damage would occur. For a strong shock wave the cell and its internal structures are compressed to the point that they fail. Evidence of this failure includes permanent deformation of organelles such as the nucleus.

The classical description of shock waves assumes they are an infinitely thin discontinuity of fluid properties. In reality, however, shock waves have a continuous structure, particularly for weak shocks relevant to TBI who fall in the acoustic regime. Within a shock wave, the typically neglected viscous shear effects are significant. The shear force is responsible for sliding fluid particles past each other. For strong shock waves, this force is large and may contribute to cell damage. Evidence of this is elongation of the cell and its features in the direction of shock wave propagation which has been documented in the past [18]. Forcibly changing the orientation of a cell will influence the structure of actin filament and may cause depolymerization. Figure 4.1 is a sketch of how the shear force can produce cell elongation in the shock wave propagation direction. On the left an undeformed cell is shown before the shock wave arrives from the right. While the shock wave passes through, shown in the middle, shear forces act to stretch the cell. After shock wave passage, the deformed cell is left behind, drawn on the right.

In order to analyze cellular modification, a common approach is to assess the effects of phenomena on the length scale of interest. The cells tested in this study have comparable

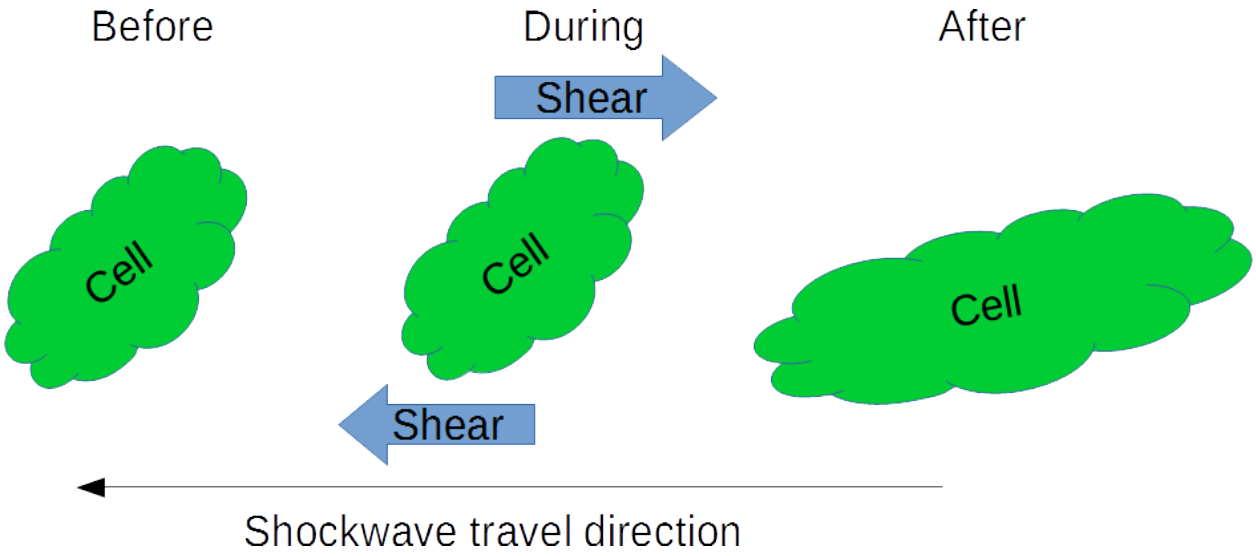

Figure 4.1: Sketch of the process to elongate a cell in the shock wave propagation direction.

sizes, all around 25 μm in diameter. This defines the length scale of interest for cells as microns. For shock waves in water with a strength of 1.7 MPa, the shock thickness has been estimated at $\sim$ 1 μm [44]. The shock thickness in weak underwater shock waves is on the micron length scale making it the quantity of interest for further analysis.

Sketched on a pressure versus position plot in Figure 4.2 is the shock thickness defined as Δ. The pressure field is given by the red curve while the vertical black lines mark the region defined as the shock thickness. The upward sloped black line is the tangent line passing through the midpoint of the red pressure trace. The end points of this line segment are located where it intersects the pre-shock and post-shock pressure, sketched as horizontal black lines. The x-projected length of this upward sloped line segment is defined as the shock thickness. The shock thickness is the area that connects pre-shock and post-shock states of a fluid. Within this layer the pressure, temperature, and density of a fluid all increase. As the shock strength, characterized by Mach number, increases, the change in fluid properties across the shock wave also increases. Unlike these properties however, the shock thickness decreases with increasing shock wave strength. This means strong shock waves have a very small shock thickness while weak waves have a larger shock thickness.

4.2 Shock Thickness Estimate

For weak shock waves Thompson has derived an equation estimating the shock thickness [45].

$$\Delta \approx \frac{8}{3} \frac{\mu_C}{(M_1 - 1)\rho_1 c_1} \tag{4.1}$$

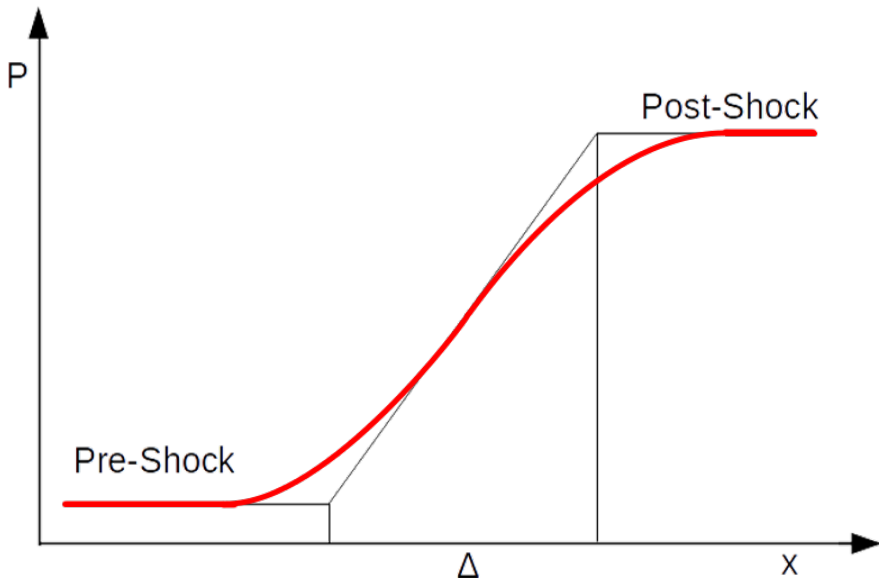

Figure 4.2: The pressure profile inside a shock transition and the definition of the shock thickness.

In (4.1), the shock thickness (Δ) depends on the fluid viscosity (μ_C), density (ρ), upstream sonic velocity (c_1), and shock wave Mach number (M_1). The viscosity in (4.1) combines bulk and shear viscosity according to (4.2).

$$\frac{4}{3}\mu_C = \frac{4}{3}\mu_{shear} + \mu_{bulk} \tag{4.2}$$

The bulk viscosity of water has been found to be $2.47 \cdot 10^{-3} Pa \cdot s$ [48]. The speed of sound, density, and shear viscosity used are 1494 $\frac{m}{s}$, 997.3 $\frac{kg}{m^3}$, and $9.1073 \cdot 10^{-4} Pa \cdot s$ respectively.

Shock pressure is a common way of characterizing shock strength as it is an easily measured property and allowed for quick comparison with previous work. It is of interest to parameterize the shock thickness using shock pressure instead of Mach number.

4.2.1 Shock Jump Equation in Water

In order to eliminate the Mach number in (4.1) and replace it with shock pressure, the shock jump equations for water need to be derived. The derivation begins with the conservation of mass, momentum, and energy flux across the shock wave, (4.3), (4.4), and (4.5).

$$\rho_1 u_1 = \rho_2 u_2 \tag{4.3}$$

$$P_1 + \rho_1 u_1^2 = P_2 + \rho_2 u_2^2 \tag{4.4}$$

$$e_1 + \frac{P_1}{\rho_1} + \frac{1}{2}u_1^2 = e_2 + \frac{P_2}{\rho_2} + \frac{1}{2}u_2^2 \tag{4.5}$$

To close the system $e(\rho, P)$ is required. Typically to describe the compressibility of water in the pressure range of up to 1000 atmospheres, the equation of state used is a modified Tait equation known as the stiffened gas equation [49]

$$e = \frac{P + \gamma P_s}{\rho(\gamma - 1)} \tag{4.6}$$

The terms in (4.6) are: pressure (P), density (ρ), internal energy (e) and two fluid constants, the stiffening pressure (P_s), and (γ). In water $P_s = 295.9$ MPa and $\gamma = 7.12$ [50].

Using the stiffened gas equation, the velocities, u_1 and u_2, can be eliminated to give (4.7) which is the locus of all post-shock states known as the Hugoniot.

$$\frac{P_2}{P_1} = \frac{v_1(\gamma + 1) - v_2(\gamma - 1) + 2\dfrac{P_s}{P_1}\gamma(v_1 - v_2)}{v_2(\gamma + 1) - v_1(\gamma - 1)} \tag{4.7}$$

Where v is specific volume. By combining (4.3) and (4.4) the Rayleigh line (4.8) was found

$$\frac{P_2}{P_1} = 1 + \frac{u_1^2}{P_1 v_1}\left(1 - \frac{v_2}{v_1}\right) \tag{4.8}$$

Equating the equation for the Raleigh line, (4.8), and Hugoniot, (4.7), defines the shock jump equation for pressure change (4.9).

$$\frac{P_2 + P_s}{P_1 + P_s} = \frac{2\gamma M_1^2 - (\gamma - 1)}{\gamma + 1} \tag{4.9}$$

Finally solving for the Mach number yields equation 4.10.

$$M_1^2 = \frac{1}{2\gamma}\left[\left(\frac{P_2 + P_s}{P_1 + P_s}\right)(\gamma + 1) + (\gamma - 1)\right] \tag{4.10}$$

Utilizing the stiffened gas equation has produced shock jump relations nearly identical to the ones found with the ideal gas law.

4.3 Scaling Law

With the shock jump equation, (4.10), and the shock thickness relation in (4.1), the shock thickness has been written as a function of the initial state fluid properties and shock pressure. With the shock thickness defined as a function of shock pressure, the scaling law anticipating cellular damage can be constructed.

The scaling law is the ratio of characteristic shock thickness to characteristic cell dimension, the cell size.

$$\frac{\Delta}{d} = \kappa \tag{4.11}$$

where d is the cell diameter and Δ is the shock thickness. There are three limiting cases of immediate interest.

The first case is when $\kappa >> 1$. This occurs when the shock thickness is much larger than the cell size, characteristic of a very weak shock passing through a cell. As the shock passes through the cell, the cell would experience uniform quasi-equilibrium loading with negligible spatial pressure gradients. The cell is compressed equally and weak shear forces try to deform the cell.

The second case is when $\kappa << 1$. A very strong shock wave characterized by its very small shock thickness applies uneven transient loading on the cell. This leads to high compressive and shear loads only affecting one part of the cell while the rest is unloaded in the pre-shock state. This creates a region of large deformation next to an undeformed area which may lead to failure of cellular structures.

The third case is when $\kappa \sim 1$ the shock thickness is comparable to the cell size. In this case the cell would experience a larger strain gradient than in the case of weak shock waves, but smaller than strong shock waves. As a result cellular modification may occur depending on the cell type. Cells in a culture dish cannot support each other three-dimensionally as *in vivo* cells are able to. This difference in environment may participate in resulting modification.

Upon reflection, the waves tested do not significantly change strength making the shock thickness nearly the same. This analysis also applies to the loading created by a reflected wave. Wave reflections in experiments which can increase damage dealt to cells through repeated loading are not accounted for in the model. Figure 4.3 shows the variation of the shock thickness as a function of shock pressure. In the graph, shock thickness decreases non-linearly with increasing shock pressure. A shock wave of about 200 kPa of pressure is predicted to have a shock thickness of 25 μm. As the shock pressure decreases below 200 kPa the shock thickness increases quickly. As the shock pressure increases above 200 kPa the shock thickness decreases to about 3 μm at 2 MPa.

Higher shock pressures, up to 10 MPa and $\kappa = 0.02$, have been obtained in exploding wire experiments. The shock thickness estimate by Thompson is made for use with weak shock waves [45]. The pressure range shown in Figure 4.3 covers up to 2 MPa and exploding wire experiments reach 10 MPa. In order to verify whether this pressure range satisfies the weak

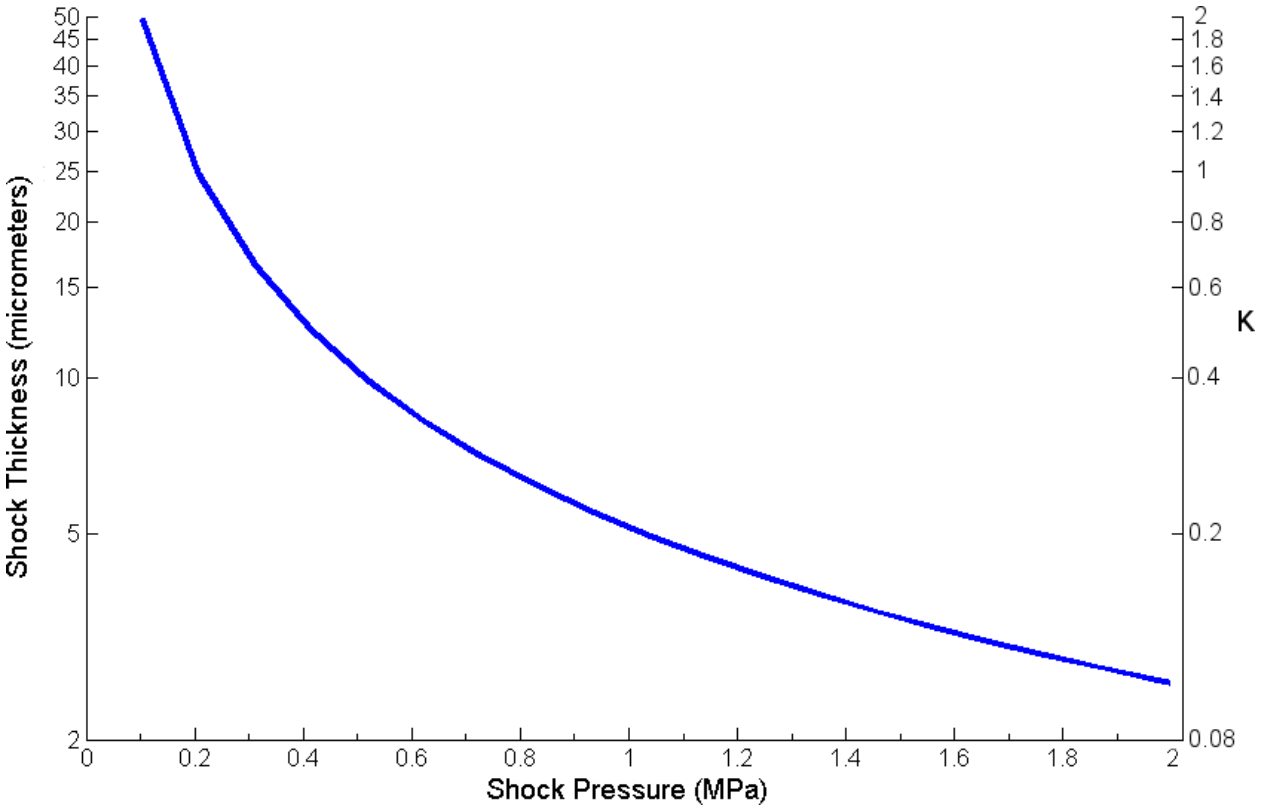

Figure 4.3: Shock thickness vs shock pressure plot for water calculated from the shock thickness estimate and using a cell size of 25 μm.

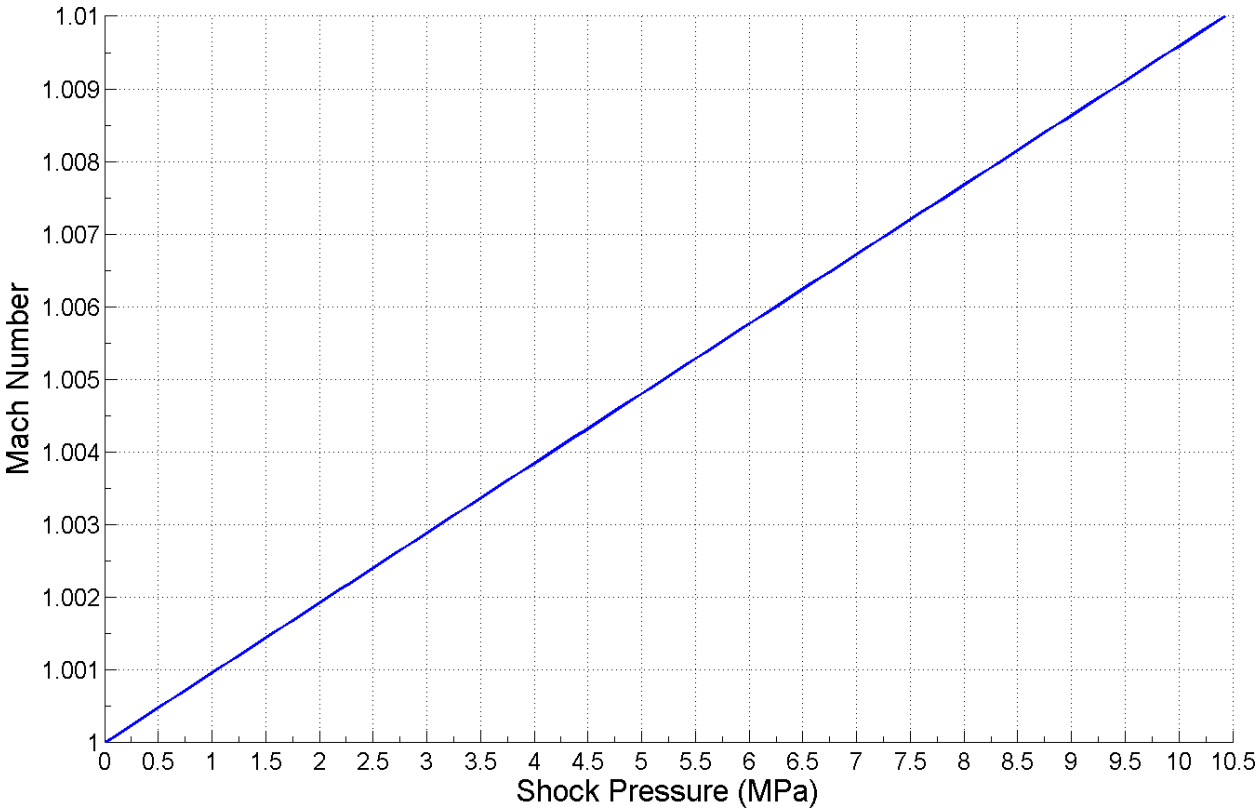

Figure 4.4: Mach number vs shock pressure plot for water.

shock wave requirement, the Mach number versus shock pressure is plotted in Figure 4.4. From the graph in Figure 4.4, a shock pressure of 10 MPa corresponds to a Mach number of 1.0095. Since this is very close to unity, the shock waves tested are indeed weak, validating use of the thickness estimate. It is of interest to determine the time it takes for the shock transition to take place. This was found by dividing the estimated shock thickness by the speed of sound. The relationship is plotted in Figure 4.5. From the graph in Figure 4.5, a shock thickness of 15 μm corresponds to a rise time of 10 ns. The largest rise time in the graph is about 35 ns which matches with a shock thickness near 50 μm. The two pressure sensors used to acquire data have rise times of 1 μs, for the wall sensor, and 4 μs, for the freefield sensor. The nanosecond time-scale of shock wave transition is much faster than the microsecond scale of sensor rise time. Therefore, it is not possible to resolve the shock wave profile with the sensors used in this study.

The scaling model developed indicates that when the cell size and shock thickness are of comparable magnitudes, cell modification may occur. The shock wave driven by reacting milled thermite was $\sim$ 300 kPa in strength with an estimated shock thickness of 20 μm. Using 3T3 cells that are about 25 μm in size, led to actin filament collapse. This result appears to coincide with the scaling model. HeLa and MDCK cells showed no change in actin filament structure suggesting the cell type cannot be neglected. The difference in these results may be related to the two cells types tested, fibroblasts and epithelial cells. HeLa and MDCK cells are epithelial cells which tend to group together and can support each other.

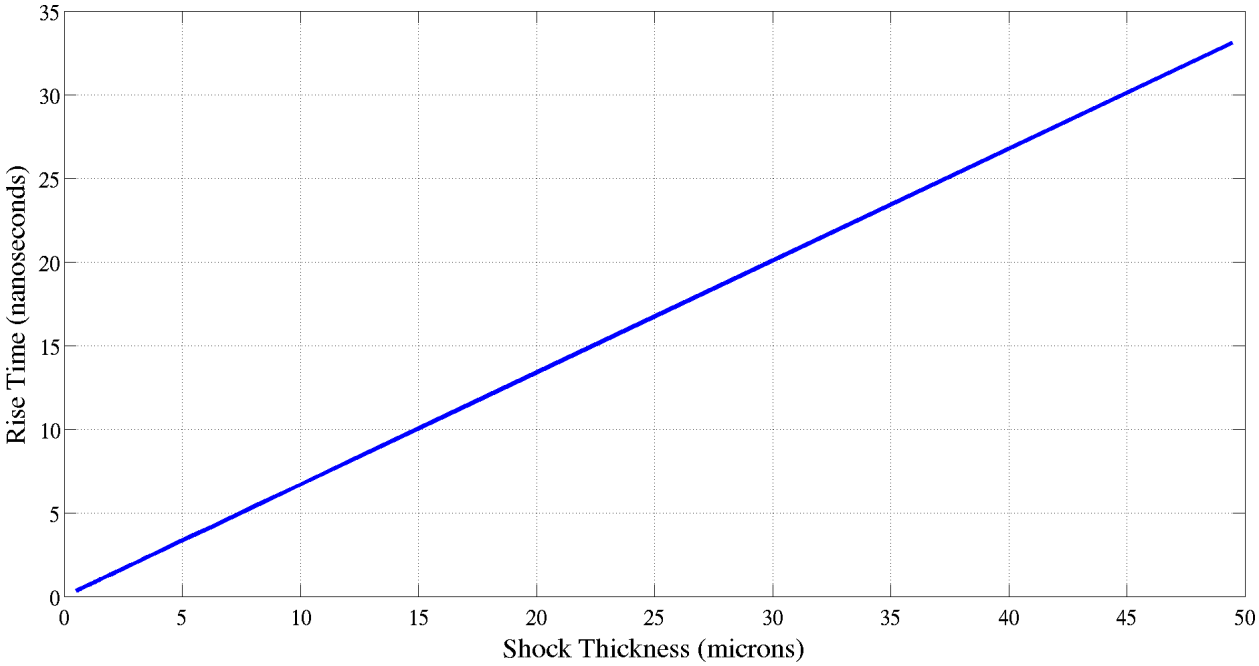

Figure 4.5: Shock rise time vs shock thickness for water.

This behavior can be most easily witnessed in MDCK cells. The epithelial cells tested did not display filament modification. In contrast, fibroblasts do not group together and the tested 3T3 cells showed microfilament change. The unmilled thermite reaction did not drive a clearly defined shock wave; however, actin collapse was still found in 3T3 cells but not in HeLa and MDCK. These findings imply modification to microfilament is caused by a mechanical phenomenon.

A 1 MPa shock wave has been previously found to produce neuronal modification in rats without hemorrhage [18]. The presented shock thickness estimate indicates this shock wave has a thickness of about 5 μm. Neuronal cell bodies are known to range from a few microns to tens of microns in diameter. As the cell size is generally larger than the shock thickness, the scaling model indicates cell modification may occur, supporting previous experimental findings of structural changes in neurons [18].

The 2 MPa shock pressure damage threshold found for lungs is known to be the lower limit for hemorrhaging [46]. A 2 MPa shock wave has a thickness of about 3 microns, which is smaller than lung cells and their $\sim$8 μm nuclei [51, 52]. The presented model suggests cell modification and damage may occur under these conditions. This is in agreement with previous findings where hemorrhaging was found [46]. It is possible lung cells will show modification similar to neurons without hemorrhage in response to a lower shock pressure.

Actin filament modification is known to be related to the activation of specific proteins within cells [32]. Future work should be focused on measuring the activity of these proteins after shock wave exposure to examine a potential biochemical pathway to filament collapse. Further work should be dedicated to closer examination of the cells tested in this preliminary study as well as other cell types. It is possible there exists a link between the level of micro-

filament collapse and imposed shock strength. This potential link can used to further drive the model presented to better explain the relationship between estimated cell dimensions, shock thickness, and cell modification. This study lays the ground work for future research from both a biological and mechanical perspective.

Chapter 5

Conclusion

The influence of pressure waves produced by reacting micron-scale aluminum copper(II)-oxide thermites on three different types of cells was investigated. Preliminary evaluations of the underwater pressure wave characteristics produced by exploding wire experiments were also completed. A model based on shock strength to predict cell modification was established and compared to experiments.

Mechanically alloyed and raw powder thermite mixtures were used to create underwater pressure waves. Both a latex barrier and silicone plug were used to trap thermite powder to protect cells. Regardless of containment method, raw powders generated weak pressure fields, ∼40 kPa max pressure, and no detectable shock wave. Milled powders drove a 300 kPa shock wave and a much larger maximum pressure at 1.5 MPa. Exploding wire tests created the greatest shock pressures at 4.2 MPa with peak pressures at 4.5 MPa. Results indicated that regardless of pressure wave loading applied from reacting thermite, only 3T3 cells showed any changes in actin filament. Immediately after exposure, microfilament was found collapsed. When allowed to recover for one hour the damaged filament reverted. In contrast, both HeLa and MDCK cells showed no change in microfilament structure.

A model comparing the shock strength, characterized by shock thickness, and cell size was established. The shock jump equations for water were derived in order to estimate the shock thickness. The scaling model predicts an underwater shock wave of 1 MPa will have a shock thickness of 5 μm. This defines the length scale for loading on a cell. For cells much larger than the shock thickness, they would experience uneven loading leading to severe mechanical deformation. When the length scales of the cell size and shock thickness were comparable, microfilament collapse was found in 3T3 cells. This shows that the shock thickness length scale is important and the mechanism behind actin modification is mechanical.

The goal of this study was to investigate the link between a pressure wave and the cells reaction on a time scale of a few hours. It was established that the cell type plays an important role in cellular response. The actin filament network of 3T3 cells was particularly sensitive to pressure waves, while HeLa and MDCK were insensitive. Preliminary results from using exploding wire to generate shock waves show pressures up to 10 MPa. This technique will enable research of cellular response to stronger shock waves. Future work should also

be directed towards connecting actin filament modification to other effects within cells and to the long-lasting macroscopic symptoms of traumatic brain injury.

Bibliography

[1] Gupta, R. and Przekwas, A., "Mathematical Models of Blast-Induced TBI: Current Status, Challenges, and Prospects," *Frontiers in Neurology*, vol. 4, no. 59, 2013. doi:10.3389/fneur.2013.00059.

[2] Clark, R.S.B. and Kochanek, P. (Eds.), "Brain Injury," *Kluwer Academic Publishers*, 2001.

[3] Wang, C., Bum Pahk, J., Balaban, C.D., and Vipperman, J.S., "Computational Study on the Bridging Vein Rupture of Blast-Induced Traumatic Brain Injury using a Numerical Human Head Model," *Proceedings of the ASME2011 International Mechanical Engineering Congress and Exposition*, 2011.

[4] Apperson, S., Thiruvengadathan, R., Bezmelnitsyn, A., Gangopadhyay, K., Gangopadhyay, S., and Polo-Parada, L., "Nanothermite-Based Microsystem for Drug Delivery and Cell Transfection. Technical Report. Defense Technical Information Center.," 2008.

[5] Dawodu, S.T., *Traumatic Brain Injury (TBI) - Definition, Epidemiology, Pathophysiology.* Medscape.

[6] Center for Disease Control and Prevention, *Heads Up: Prevent Shaken Baby Syndrome.* 2015. http://www.cdc.gov/concussion/HeadsUp/sbs.html.

[7] DeKosky, S.T., Ikonomovic, M. D., and Gandy, S., "Traumatic Brain Injury - Football, Warfare, and Long-Term Effects.," *Cytoskeleton. (Hoboken, N.J.)*, vol. 67, no. 10, pp. 630–634. doi:10.1002/cm.20475, 2010.

[8] Marikar, S., "Natasha Richardson Died of Epidural Hematoma After Skiing Accident. ABC News. March 19, 2009. http://abcnews.go.com/Entertainment/Movies/story?id=7119825."

[9] Nakagawa, A. and Manley, G.T. and Gean, A.D. and Ohtani, K. and Armonda, R. and Tsukamoto, A. and Yamamoto, H. and Takayama, K. and Tominaga, T., "Mechanisms of Primary Blast-Induced Traumatic Brain Injury: Insights from Shock-Wave Research," *Journal of Neurotrauma*, vol. 28, pp. 1101–1119, June 2011.

[10] Warden, D., "Military TBI During the Iraq and Afganistan Wars," *Journal of Head Trauma*, vol. 21, no. 5, pp. 398–402, 2006.

[11] Tanielian, T. and Jaycox, L.H. (eds.), *Invisible Wounds of War: Psychological and Cognitive Injuries, Their Consequences, and Services to Assist Recovery.* Center for Military Health Policy Research. RAND Corporation, 2008.

[12] Ramasay, A., Hill, A.M., Clasper, J.C., "Improvised Explosive Devices: Pathophysiology, Injury Profiles and Current Medical Management," *Journal of the Royal Army Corps*, vol. 155, no. 4, pp. 265–272. doi:10.1136/jramc–155–04–05, 2009.

[13] Xi, X. and Zhong, P., "Dynamic Photoelastic Study of the Transient Stress Field in Solids during Shock Wave Lithotripsy," *The Journal of the Acoustical Society of America*, vol. 109, no. 3, pp. 1226–1239. http://dx.doi.org/10.1121/1.1349183, 2001.

[14] Smith, D.H. and Meaney, D.F., "Axonal Damage in Traumatic Brain Injury," *The Neuroscientist*, vol. 6, no. 6, pp. 483–495. doi:10.1177/107385840000600611, 2000.

[15] Margulles,S., "The Postconcussion Syndrome After Mild Head Trauma: Is Brain Damage Overdiagnosed? Part 1," *Journal of Clinical Neuroscience*, vol. 7, no. 5, pp. 400–408. DOI: 10.1054/ jocn.1999.0681,, 2000.

[16] Cernak, I.,, "The Importance of Systemic Response in the Pathobiology of Blast-induced Neurotrauma," *Frontiers in Neurology*, vol. 1, no. 151, p. doi: 10.3389/fneur.2010.00151, 2010.

[17] Cernak, I., Wang, Z., Jiang, J., Bian, X., and Savic, J., "Ultrastructural and Functional Characteristics of Blast Injury-nduced Neurotrama," *Journal of Trauma Injury, Infection, and Critical Care*, vol. 50, no. 4, pp. 695–706, 2000.

[18] Kato, K. and Fujimura, M. and Nakagawa, A. and Saito, A. and Ohki, T. and Takayama, K. and Tominaga, T., "Pressure-dependent Effect of Shock Waves on Rat Brain: Induction of Neuronal Apoptosis Mediated by a Caspase-dependent Pathway," *Journal of Neurosurgery*, vol. 106, pp. 667–676, April 2007.

[19] Kaur, C., Singh, J., Lim, M.K., Ng, B.L., Yap, E.P.H., and Ling, E.A., "The Response of Neurons and Microglia to Blast Injury in the Rat Brain," *Neuropathology and Applied Neurobiology*, vol. 21, pp. 369–377, 1995.

[20] Nakagawa, A. and Kusaka, Y. and Hirano, T. and Saito, T. and Shirane, R. and Takayama, K. and Yoshimoto, T., "Application of Shock Waves as a Treatment Modality in the Vicinity of the Brain and Skull," *Journal of Neurosurgery*, vol. 99, pp. 156–162, July 2003.

[21] Nakagawa, A., Fujimura, M., Kato, K., Okuyama, H., Hashimoto, T., Takayama, K., Tominaga, T., "Shock Wave-induced Brain Injury in Rat: Novel Traumatic Brain Injury Animal Model," *Acta Neurochirurgica Supplements*, vol. 102, pp. 421–424, 2009.

[22] Tamagawa, M. and Akamatsu, T., "Effects of Shock Waves on Living Tissue Cells and its Deformation Process Using a Mathematical Model," *JSME International Journal*, vol. 42, no. 3, pp. 640–647, 1999.

[23] Bowen, I.G., Fletcher, E.R., Richmond, D.R., Hirsch, F.G., and White, C.S., "Biophysical Mechanisms and Scaling Procedures Applicable in Assessing Responses of the Tho-

rax Energized By Air-blast Overpressures or by Nonpenetrating Missiles," *Annals of the New York Academy of Sciences*, vol. 152, no. 1, pp. 122–146, 1968. DOI: 10.1111/j.1749-6632.1968.tb11971.x.

[24] Leaning, M.S., Pullen, H.E., Carson, E.R., Al-Dahan, M., Rajkumar, N., and Finkelstein, L., "Modelling a complex biological system: the human cardiovascular system 2. Model validation, reduction and development ," *Transactions of the Institute of Measurement and Control*, vol. 5, pp. 87–98, 1983.

[25] Leaning, M.S., Pullen, H.E., Carson, E.R., and Finkelstein, L., "Modelling a complex biological system: the human cardiovascular system1. Methodology and model description," *Transactions of the Institute of Measurement and Control*, vol. 5, pp. 71–86, 1983.

[26] Takhounts, E.G., Eppinger, R.H., "On the Development of the SIMon Finite Element Head Model," *Stapp Car Crash Journal*, vol. 47, pp. 107–133, 2003.

[27] Zhong, P., Zhou, Y., Zhu, S., "Dynamics of Bubble Oscillation in Contrained Media and Mechanisms of Vessel Rupture in SEL," *Ultrasound in Medicine and Biology*, vol. 27, no. 1, pp. 119–134, 2001.

[28] Haase, K. and Pelling, A.E., "Investigating Cell Mechanics with Atomic Force Microscopy," *Journal of The Royal Society Interface*, vol. 12, 2015. doi: 10.1098/rsif.2014.0970.

[29] LaPlaca, M.C., Cullen, D.K., McLoughlin, J.J., Cargill II, R.S., "High Rate Shear Strain of Three-Dimensional Neural Cell Cultres: A New In Vitro Traumatic Brain Injury Model," *Journal of Biomechanics*, vol. 38, no. 5, pp. 1093–1105. doi:10.1016/j.jbiomech.2004.05.032, 2004.

[30] Pfister, B.J., Weihs, T.P., Betenbaugh, M., and Bao, G., "An In Vitro Uniaxial Stretch Model for Axonal Injury," *Annals of Biomedical Engineering*, vol. 31, no. 5, pp. 589–598. doi:10.1114/1.1566445, 2003.

[31] Maines, G., "Nanothermite Research for Cellular Modification. M.A.Sc Thesis. University of Ottawa," 2013.

[32] Lodish, H., Berk, A., Matsudaira, P., Kaiser, C.A., Krieger, M., Scott, M.P., Zipursky, S.L., and Darnell, J., *Molecular Cell Biology*. W.H. Freeman and Company, 5th ed., 2004.

[33] Watanabe-Nakayama, T., Machida, S., Harada, I., Sekiguchi, H., Afrin, R., and Ikai, A., "Direct Detection of Cellular Adaptation to Local Cyclic Stretching at the Single Cell Level by Atomic Force Microscopy," *Biophysical Journal*, vol. 100, no. 3, pp. 564–573, 2011.

[34] R. Bhattacharjee, "Experimental Investigation of Detonation Re-initiation Mechanisms Following a Mach Reflection of a Quenched Detonation. M.A.Sc Thesis. University of Ottawa," 2013.

[35] National Center for Biotechnology Information. U.S. National Library of Medicine. PubMed, "3T3 cell," 2015. [Online; accessed 04-November-2015].

[36] National Center for Biotechnology Information. U.S. National Library of Medicine. PubMed, "HeLa cell," 2015. [Online; accessed 04-November-2015].

[37] National Center for Biotechnology Information. U.S. National Library of Medicine. PubMed, "MDCK cell," 2015. [Online; accessed 04-November-2015].

[38] Todaro, G.J. and Green, H., "Quantitative Studies of the Growth of Mouse Embryo Cells in Culture and their Development into Established Lines," *Journal of Cell Biology*, vol. 17, pp. 299–313, 1963.

[39] Scherer, W.F., Syverton, J.T., and Gey, G.O., "Studies On The Propagation In Vitro Of Poliomyelitis Viruses," *Journal of Experimental Medicine*, vol. 97, no. 5, pp. 695–710, 1953.

[40] Puck, T.T. and Marcus, P.I., "A Rapid Method For Viable Cell Titration and Clone Production With HeLa Cells in Tissue Cultrue: The Use of X-Irradiated Cells to Supply Conditioning Factors," *Proceedings of the National Academy of Sciences of the United States of America*, vol. 41, no. 7, pp. 432–437, 1955.

[41] Davidson, M.W., "Madin-Darby Canine Kidney Epithelial Cells (MDCK Line). Fluorescence Digital Image Gallery. Florida State University," 2013.

[42] Dukes, T.D., Whitley, P. and Chalmers, A.D., "The MDCK Variety Pack: Choosing the Right Strain," *BMC Cell Biology*, vol. 12, no. 43, pp. doi:10.1186/1471–2121–12–43, 2011.

[43] Lugovtsev, V.Y. Meinyk, D. and Weir, J.P., "Heterogeneity of the MDCK Cell Line and Its Applicability for Influenza Virus Research," *Plos One*, vol. 8, no. 9, 2013.

[44] Flook Jr, W.M., and Hornig, D.F., "The Experimental Determination of the Thickness of Weak Shock Fronts in Liquids," *Brown University. Armed Services Technical Information Agency. Technical Report No. 5*, 1964.

[45] Thompson, P.A., *Compressible-Fluid Dynamics*. Philip A. Thompson, 1988.

[46] Delius, M., Enders, G., Heine, G., Stark, J., Remberger, K., and Brendel, W., "Biological Effects of Shock Waves: Lung Hemorrhage by Shock Waves in Dogs–Pressure Dependence," *Ultrasound in Medicine and Biology*, vol. 13, no. 2, pp. 61–67, 1987.

[47] Mayer, R., Schenik, E., Child, S., Norton, S., Cox, C. Hartman, C., Cox, C., and Carstensen, E., "Pressure threshold for shock wave induced renal hemorrhage," *The Journal of Urology*, vol. 144, no. 6, pp. 1505–1509, 1990.

[48] Holmes, M.J., Parker, N.G., and Povey, M.J.W., "Temperature Dependence of Bulk Viscosity in Water using Acoustic Spectroscopy," *Journal of Physics: Conference Series*, vol. 269, p. arXiv:1002.3029, 2010.

[49] R. Menikoff and Y. E. Horie, *Stiffened Gas EOS*, ch. 4.3.2 in Shock Wave Science and Technology Reference Library Volume 2. Springer, Berlin, 2007.

[50] Nakahara, M., Nagayama, K., and Mori, Y., "Shockwave Dynamics of High Pressure Pulse in Water and Other Biological Materials Based on Hugoniot Data," *Japanese Journal of Applied Physics*, vol. 47, no. 5, pp. 3510–3517, 2008.

[51] Stone, K.C., Mercer. R.R., Gehr, P., Stockstill, B., and Crapo, J.D., "Allometric Relationships of Cell Numbers and Size in the Mammalian Lung," *American Journal of Respiratory Cell and Molecular Biology*, vol. 6, no. 2, pp. 235–243. doi:10.1165/ajrcmb/6.2.235, 1992.

[52] Crapo, J.D., Barry, B.E., Gehr, P., Bachofen, M., and Weibel, E.R., "Cell Number and Cell Characteristics of the Normal Human Lung," *The American Review of Respiratory Disease*, vol. 126, no. 2, pp. 332–337, 1982.

APPENDICES

Appendix A

Derivation of Shock Jump Equations for the Stiffened Gas Equation of State

We want to determine the shock jump equations for underwater shock waves. In order to do this we will focus on flow through a one dimensional steady shock wave. We will choose a control volume far away from the shock front so that viscous effects and heat transfer can be neglected. The conservation of mass, momentum and, energy for steady one-dimensional flow have the form

$$\rho_1 u_1 = \rho_2 u_2 \tag{A.1}$$

$$P_1 + \rho_1 u_1^2 = P_2 + \rho_2 u_2^2 \tag{A.2}$$

$$e_1 + \frac{P_1}{\rho_1} + \frac{1}{2}u_1^2 = e_2 + \frac{P_2}{\rho_2} + \frac{1}{2}u_2^2 \tag{A.3}$$

Using the conservation of mass, (A.1), we can eliminate u_2 from the conservation of momentum and energy, (A.2) and (A.3)

$$P_2 - P_1 = \rho_1 u_1^2 \left(1 - \frac{\rho_1}{\rho_2}\right) \tag{A.4}$$

$$e_2 - e_1 = \frac{P_1}{\rho_1} - \frac{P_2}{\rho_2} + \frac{u_1^2}{2}\left(1 - \frac{\rho_1}{\rho_2}\right)\left(1 + \frac{\rho_1}{\rho_2}\right) \tag{A.5}$$

Combining (A.4) and (A.5) gives

$$e_2 - e_1 = \frac{1}{2}(P_1 + P_2)\left(\frac{1}{\rho_1} - \frac{1}{\rho_2}\right) \tag{A.6}$$

Replacing density with specific volume yields

$$e_2 - e_1 = \frac{1}{2}(P_1 + P_2)(v_1 - v_2) \tag{A.7}$$

This rewritten form of the governing equations relates internal energy, pressure and, density of any general fluid. Now the siffened gas equation of state will be introduced which is often used in analyzing explosions underwater. This equation has the form

$$e\rho(\gamma - 1) = P + \gamma P_s \tag{A.8}$$

One can see this is simplify a modified form of the ideal gas law a new parameter called the stiffening pressure P_s. In addition γ is also a fitting constant instead of the isentropic exponent. This equation is useful because it produces flow relations very similar to those produced using the ideal gas law. Rearranging the stiffened gas equation yields

$$e = v\frac{P + \gamma P_s}{\gamma - 1} \tag{A.9}$$

Now we will use the stiffened gas equation along with the equations of fluid motion to define the Rayleigh line and Hugoniot. First, removing the internal energy from (A.6) yields

$$v_2\frac{P_2 + \gamma P_s}{\gamma - 1} - v_1\frac{P_1 + \gamma P_s}{\gamma - 1} = \frac{1}{2}(P_1 + P_2)(v_1 - v_2) \tag{A.10}$$

Cleaning up the denominators

$$2v_2(P_2 + \gamma P_s) - 2v_1(P_1 + \gamma P_s) = P_1(v_1 - v_2)(\gamma - 1) + P_2(v_1 - v_2)(\gamma - 1) \tag{A.11}$$

Grouping together the terms multiplied by P_1 and P_2

$$2P_2v_2 - P_2v_1(\gamma - 1) + P_2v_2(\gamma - 1) = P_1(v_1 - v_2)(\gamma - 1) + 2P_1v_1 - 2P_sv_2\gamma + 2P_sv_1\gamma \tag{A.12}$$

Simplifying

$$P_2(v_2(\gamma + 1) - v_1(\gamma - 1)) = P_1(v_1(\gamma + 1) - v_2(\gamma - 1)) + 2P_s\gamma(v_1 - v_2) \tag{A.13}$$

Diving both sides by P_1 and rearranging gives the Hugoniot

$$\frac{P_2}{P_1} = \frac{v_1(\gamma + 1) - v_2(\gamma - 1) + 2\dfrac{P_s}{P_1}\gamma(v_1 - v_2)}{v_2(\gamma + 1) - v_1(\gamma - 1)} \tag{A.14}$$

Taking (A.4) and rewriting it in terms of $\dfrac{P_2}{P_1}$ gives

$$\frac{P_2}{P_1} - 1 = \frac{u_1^2}{P_1v_1}\left(1 - \frac{v_2}{v_1}\right) \tag{A.15}$$

$$\frac{P_2}{P_1} = 1 + \frac{u_1^2}{P_1v_1}\left(1 - \frac{v_2}{v_1}\right) \tag{A.16}$$

This is the equation of the Raleigh line

(A.17)

Equating the Raleigh line and Hugoniot will allow us to determine for the shock jump equation for density changes.

$$1 + \frac{u_1^2}{P_1 v_1}\left(1 - \frac{v_2}{v_1}\right) = \frac{(\gamma+1) - \frac{v_2}{v_1}(\gamma-1) + 2\gamma\frac{P_s}{P_1}\left(1 - \frac{v_2}{v_1}\right)}{\frac{v_2}{v_1}(\gamma+1) - (\gamma-1)} \tag{A.18}$$

Solving this using Mathematica for $\frac{v_2}{v_1}$ gives

$$\frac{v_2}{v_1} = \frac{2\gamma\left(1 + \frac{P_s}{P_1}\right) + (\gamma-1)\frac{u_1^2}{P_1 v_1}}{(\gamma+1)\frac{u_1^2}{P_1 v_1}} \tag{A.19}$$

Introducing the Mach number

$$\frac{v_2}{v_1} = \frac{2\gamma\left(1 + \frac{P_s}{P_1}\right) + (\gamma-1)\frac{M_1^2 c_1^2}{P_1 v_1}}{(\gamma+1)\frac{M_1^2 c_1^2}{P_1 v_1}} \tag{A.20}$$

The speed of sound in the siffened gas equation of state is given by

$$c^2 = \gamma v(P + P_s) \tag{A.21}$$

Replacing the speed of sound gives

$$\frac{v_2}{v_1} = \frac{2\gamma\left(1 + \frac{P_s}{P_1}\right) + (\gamma-1)\frac{M_1^2\gamma v_1(P_1+P_s)}{P_1 v_1}}{(\gamma+1)\frac{M_1^2\gamma v_1(P_1+P_s)}{P_1 v_1}} \tag{A.22}$$

Cleaning up

$$\frac{v_2}{v_1} = \frac{2\gamma\left(1 + \frac{P_s}{P_1}\right) + (\gamma-1)M_1^2\gamma\left(1 + \frac{P_s}{P_1}\right)}{(\gamma+1)M_1^2\gamma\left(1 + \frac{P_s}{P_1}\right)} \tag{A.23}$$

$$\frac{v_2}{v_1} = \frac{2 + (\gamma-1)M_1^2}{(\gamma+1)M_1^2} \tag{A.24}$$

We have recovered a density change using the stiffened gas relation that is identical to the density change across a shock using the ideal gas equation. We will now determine the pressure jump using this and the Raleigh line.

$$\frac{P_2}{P_1} = 1 + \frac{u_1^2}{P_1 v_1}\left(1 - \frac{v_2}{v_1}\right) \tag{A.25}$$

Inserting the Mach number and density jump gives

$$\frac{P_2}{P_1} = 1 + \gamma M_1^2\left(1 + \frac{P_s}{P_1}\right)\left(1 - \frac{2 + (\gamma - 1)M_1^2}{(\gamma + 1)M_1^2}\right) \tag{A.26}$$

This is the pressure jump across a shockwave however, it is hard to compare this to the ideal gas form. Multiplying through by P_1 and adding P_s to both sides gives

$$P_2 + P_s = P_1 + P_s + \gamma M_1^2(P_1 + P_s)\left(1 - \frac{2 + (\gamma - 1)M_1^2}{(\gamma + 1)M_1^2}\right) \tag{A.27}$$

Arranging all the pressure terms on the left and simplifying the right gives

$$\frac{P_2 + P_s}{P_1 + P_s} = 1 + \gamma M_1^2\left(1 - \frac{2 + (\gamma - 1)M_1^2}{(\gamma + 1)M_1^2}\right) \tag{A.28}$$

$$\frac{P_2 + P_s}{P_1 + P_s} = \frac{2\gamma M_1^2 - (\gamma - 1)}{\gamma + 1} \tag{A.29}$$

The right side here is the same as the ideal gas pressure jump equation. However the left side now contains the stiffening pressure. Expressing the pressure jump without the stiffening pressure yields

$$P_2 = (P_1 + P_s)\left(\frac{2\gamma M_1^2 - (\gamma - 1)}{\gamma + 1}\right) - P_s \tag{A.30}$$

$$\frac{P_2}{P_1} = \left(1 + \frac{P_s}{P_1}\right)\left(\frac{2\gamma M_1^2 - (\gamma - 1)}{\gamma + 1}\right) - \frac{P_s}{P_1} \tag{A.31}$$

It is of interest to determine the upstream Mach number as a function of the pressure jump. This can be easily found by solving (A.29) for Mach number to give

$$M_1^2 = \frac{1}{2\gamma}\left[\left(\frac{P_2 + P_s}{P_1 + P_s}\right)(\gamma + 1) + (\gamma - 1)\right] \tag{A.32}$$

With the shock jump equations defined it is now possible to use the shock thickness estimate found by Thompson [45].

$$\frac{8}{3}\frac{\mu_C}{\rho_1 c_1 \Delta} \approx M_1 - 1 \tag{A.33}$$

μ_C is the combined bulk and shear viscosity defined as

$$\frac{4}{3}\mu_C = \frac{4}{3}\mu_{shear} + \mu_{bulk} \tag{A.34}$$

Solving for Δ gives

$$\Delta \approx \frac{8}{3}\frac{\mu_C}{(M_1 - 1)\rho_1 c_1} \tag{A.35}$$

Appendix B

MATLAB Code

B.1 Low-Pass Filter

```
% This program performs low-pass filtering using an equiripple filter
% Input: pressure - the pressure data to be filtered
% Input: samplingRate - the sampling rate in Hz used to collect data
% Output: filtered - the filtered data
function [filtered] = SignalFilter(pressure,samplingRate)
   passStart = 0.1/2; % Define the frequency in Hz of the start of the pass band
   passEnd = 500000/2; % Define the frequency in Hz of the end of the pass band
   % The frequencies are divided by two because the filter uses one-half of the
       given sampling rate to normalize all frequencies.

   ripple = 1; % Define in dB the pass-band ripple
   atten = 60; % Define in dB the stop-band attenuation

    PassOne = fdesign.lowpass(passStart,passEnd,ripple,atten,samplingRate);
    % Provide filter parameters

    HD = design(PassOne);  % Create the filter
    filtered = filter(HD,pressure); % Filter the data
end
```

B.2 Calculation of Frequency Content

```
% This program uses the fast Fourier transform (FFT) to determine frequency
    content of a given signal
% Input: data - the sample to be analyzed
% Input: samplingRate - the sampling rate in Hz used to acquire the sample
% Output: a graph of power spectral density vs frequency
function findFrequencyContent(data,samplingRate)
    dims = size(data,1); % Get the number of data points in the sample
    dataFFT = fft(data); % Perform FFT on the data
    powDen = dataFFT.*conj(dataFFT)/dims; % Calculate the spectral power density
    xAxis = samplingRate/dims*(1:dims); % Form the x-axis of the graph
    fig = figure; % Make a figure to hold the graph
    hold on;
    plot(xAxis/1000,powDen); % Draw the graph
    xlabel('Frequency (kHz)'); % Label the x-axis
    ylabel('Power'); % Label the y-axis
    title('Spectral Power Density'); % Add a title to the graph
    hold off;
end
```